Reaction and microstructure development of one-part geopolymer for wellbore applications

An experimental and numerical study

Gupta, Mayank; Qiu, Xiujiao; Omran, Mohamed; Chen, Yun; Khalifeh, Mahmoud; Ye, Guang

DOI
10.1016/j.cemconres.2024.107738

Publication date
2025

Document Version
Final published version

Published in
Cement and Concrete Research

Citation (APA)
Gupta, M., Qiu, X., Omran, M., Chen, Y., Khalifeh, M., & Ye, G. (2025). Reaction and microstructure development of one-part geopolymer for wellbore applications: An experimental and numerical study. *Cement and Concrete Research*, *188*, Article 107738. https://doi.org/10.1016/j.cemconres.2024.107738

Cement and Concrete Research 188 (2025) 107738

Contents lists available at ScienceDirect

Cement and Concrete Research

journal homepage: www.elsevier.com/locate/cemconres

Reaction and microstructure development of one-part geopolymer for wellbore applications – An experimental and numerical study

Mayank Gupta [a,*], Xiujiao Qiu [a], Mohamed Omran [b], Yun Chen [a], Mahmoud Khalifeh [b], Guang Ye [a]

[a] Department of Materials, Mechanics, Management & Design, Delft University of Technology, Delft, 2628, CN, the Netherlands
[b] Department of Energy and Petroleum Engineering, University of Stavanger, Stavanger 4036, Norway

ARTICLE INFO

Keywords:
Alkali activated materials
Reaction and transport
Microstructure
Carbon capture and storage
Numerical simulation
Thermodynamic modeling

ABSTRACT

This study focuses on the numerical modeling of the reaction and microstructure development of a one-part granite-based geopolymer, which is often used for carbon capture and storage (CCS) applications. This work extends the capabilities of GeoMicro3D to model one-part geopolymers containing different precursors and activators (solid and in solution). The model considers the particle size distribution of different solids and the real shape of particles to prepare the initial simulation domain. Further, the dissolution rates of different solids estimated from the experiments were used to model the dissolution of different elements in the pore solution. Subsequently, the model utilizes classical nucleation probability modeling coupled with thermodynamic modeling to estimate the precipitation of products in the microstructure. Experiments were performed to study the pore solution, reaction degree, and amount of products in the microstructure, which were further compared with the simulation results to check the rationality of the model.

1. Introduction

Due to the increasing concentration of greenhouse gases such as CO_2 and methane (CH_4) in the atmosphere, carbon capture and storage (CCS) strategies have become very crucial [1,2]. The Intergovernmental Panel on Climate Change (IPCC) report has acknowledged that CCS in existing underground geological formations (gas fields and ocean storage) has the potential to stabilize atmospheric CO_2 concentrations [3,4]. The well sealant integrity is the main challenge during the injection operation and for the long-term storage of CO_2 [5,6]. The main integrity issues include mechanical failure and chemical degradation, which creates leakage in pathways for CO_2 [7–9]. Conventionally used Ordinary Portland Cement (OPC) has been observed to have brittle mechanical failure and undergo faster degradation, which increases the porosity and permeability of sealant [10–13]. Many alternatives for the OPC, such as calcium sulfoaluminate cement, alkali-activated materials, and calcium aluminate cement, have been studied for CCS applications [14–16]. Geopolymers have come out to be effective due to their higher flexibility, excellent acid-resistant characteristics, good resistance to freeze-thaw cycles, and durability in harsh environments [17–22].

The recently developed rock-based geopolymers (containing granite, aplite, and norite) have been studied for downhole applications (for CCS) due to their setting behavior, lower permeability, bonding to steel and formation, higher mechanical performance, lower chemical shrinkage, compatibility with oil-base drilling fluids and higher strength/modulus ratios [23–27]. In addition to this, the abundant availability, cost-effectiveness, and low carbon footprint of this material make it an attractive alternative to traditional cementitious materials, further emphasizing its potential for large-scale implementation in CCS projects.

The long-term integrity and mechanical properties of any materials are dependent on the microstructure, reaction products, and chemical properties of the materials, which are often measured through dedicated experiments [28–30]. However, with the advent of computer technologies and better computing facilities, numerical models have also become an alternative path to study the chemical and physical properties of the materials. Different numerical models have been developed, such as CEMHYD3D, HYMOSTRUC, and μic, which simulate the chemical reaction and microstructure development of OPC-based materials [31–34]. To the best of the authors' knowledge, currently, GeoMicro3D has the capability to model the chemical reactions and microstructure development for alkali activated materials [35,36]. GeoMicro3D has

* Corresponding author.
E-mail address: mayank.gupta.civ13@iitbhu.ac.in (M. Gupta).

https://doi.org/10.1016/j.cemconres.2024.107738
Received 2 August 2024; Received in revised form 18 October 2024; Accepted 21 November 2024
Available online 26 November 2024

been developed to model the reaction and microstructure of the two-part alkali-activated slag. However, simulation models for the hydration and microstructure development of one-part geopolymers are not available. Additionally, the one-part granite-based geopolymer developed for the CCS application has additional components such as micro silica, solid activator (K_2SiO_3), and granite rock in the mix, which further complicates the system [23,26]. In order to address the above shortcomings, the current work specifically focuses on the development of the numerical model for the one-part geopolymers. The objective of the current study was to extend the GeoMicro3D to simulate the dissolution of different components of the one-part geopolymer and thermodynamically model the precipitation of the different products. From the modeling perspective, the input simulation domain is created by distributing the different solids in the simulation domain, considering the real shape of the particles and particle size distribution of the different solids. Dedicated experiments were performed to measure the dissolution rates of different components (precursors and activators), which were further used as input for the numerical model. Notably, the one-part granite-based geopolymers refers that one of the components is granite, however due to low reactivity at room temperatures, it is considered inert in the modeling and has not been investigated for dissolution experiments. Following the dissolution of solids, the transport of the ion in the microstructure was modeled using the Lattice Boltzmann Method (LBM). Lastly, the model was coupled with GEMS to thermodynamically model the precipitation of the different reaction products. Further experiments were carried out at the paste level to study the pore solution and microstructure of the geopolymer paste and compare the model output with the experimental data.

In this article, the details about the raw materials, mix design, and different experiments are outlined in Section 2. Further, the detailed description of different modules and formulations used in the numerical model is described in Section 3. Finally, the experimental results are discussed, and the validity of the model is checked by comparing it with experimental data in Section 4.

2. Materials and experimental methods

2.1. Materials and mix design

The main raw materials used in the current study as precursors for this one part geopolymer are Ground Granulated Blast Furnace Slag (GGBFS), micro-silica, and granite (mainly containing quartz, K-feldspars, and biotite). The chemical compositions of the slag, micro silica, and granite were measured through X-ray fluorescence and are listed in Table 1. The mineral composition of the granite used was determined by Rietveld analysis and is shown in Table 2. The specific gravities of the slag, micro silica, and granite used in this study are 2.90, 2.25, and 2.63, respectively.

The particle size distributions of the raw materials (slag, granite, K_2SiO_3, micro silica) used in the current study are given in Fig. 1. The activator used was a combination of *KOH* and K_2SiO_3. The concentration of KOH used for the mixture is 1.86 mol/lit. The mix proportion of the geopolymer paste used in the current study is given in Table 3. Further information about the development of this geopolymer is explained in the literature [23,24,26].

2.2. Experimental methods

This section elaborates on different experiments carried out to calculate different material parameters for the inputs to the simulation model (GeoMicro3D) and also to validate the model.

2.2.1. Particle dissolution - ICP-OES analysis

This experiment was carried out to calculate the forward dissolution rates of different solids used in the mix. The forward dissolution rates of slag, micro-silica, and potassium silicate were then determined by dissolving 0.1 g of solid in 100 mL of alkaline solution. The alkaline solution was prepared with potassium hydroxide by mixing it in 4 different concentrations, namely 0.1, 0.5, 1.0, and 2.0 mol/L, resulting in the pH values of 12.89, 13.54, 13.88, and 14.22, respectively. Such a high pH of the solution also ensures the negligible effect of alkalinity caused by the slag on dissolution kinetics. The solutions were continuously stirred at 250 rpm using a magnetic stirrer in a polystyrene container at 17–23 °C. The high liquid/solid ratio ensures that the solution was significantly diluted and that no products are formed so that the obtained dissolution rate was the forward dissolution rate. During the dissolution process, small samples of the solution were taken after 5, 15, 30, 60, 120, 240, and 1220 mins (set time intervals). Then, the sampled solutions were diluted using nitric acid (0.2 vol%). The diluted solutions were analyzed using a spectrometer to determine the concentrations of Si, Al, and Ca. A PerkinElmer Optima 5300DV ICP-OES spectrometer was used to measure the concentration of the ions from the diluted solutions.

The forward dissolution rate (r_{X+}) of any element X for any solids was estimated using the following equation:

$$r_{X+} = \frac{d[X]}{dt}\left(\frac{V}{m.SSA}\right) \quad (1)$$

where $\frac{d[X]}{dt}$ denotes the rate of dissolution (mol/m^{3}s) of ion X and V, m and SSA represent the solution volume (m^3), mass of the solid (kg), and specific surface area of the solid (m^2/kg), respectively.

2.2.2. Pore solution analysis

Pore solution analysis was conducted at the paste scale to measure the elemental concentration of the pore solution and to compare it with the simulated pore solution composition. For the pore solution extraction, cylindrical specimens with a diameter of 34 mm and height of 70 mm were used. Pore solutions of the hardened geopolymer specimens were extracted by inserting the specimen into the hollow steel cylinder. After the pore solution extraction, the solution was filtered using a 0.45 μm syringe filter. The pore solution of the cement paste was extracted after 12 h, 1, 3, 7, and 14 days of curing. The concentration of the Ca, Si, Al, Mg, K, and Na in the solution was measured using ICP-OES.

Table 1
Chemical compositions (wt%) of the precursors used in this study.

Precursors	SiO_2	Al_2O_3	Fe_2O_3	MgO	CaO	Na_2O	K_2O	TiO_2	MnO	LOI
Slag	35.78	12.72	0.18	12.77	33.74	0.55	0.82	2.23	0.58	0.3
Micro silica	100	–	–	–	–	–	–	–	–	–
Granite	73.44	13.33	2.06	0.44	1.12	3.12	5.11	0.23	0.04	0.9

Table 2
Mineral composition of granite rock used in this study.

Minerals	Feldspar (%)	Quartz (%)	Plagioclase (%)	Muscovite (%)	Biotite (%)	Chlorite (%)	Total (%)
Granite	44.3	30.4	5.1	4.9	3.5	11.8	100

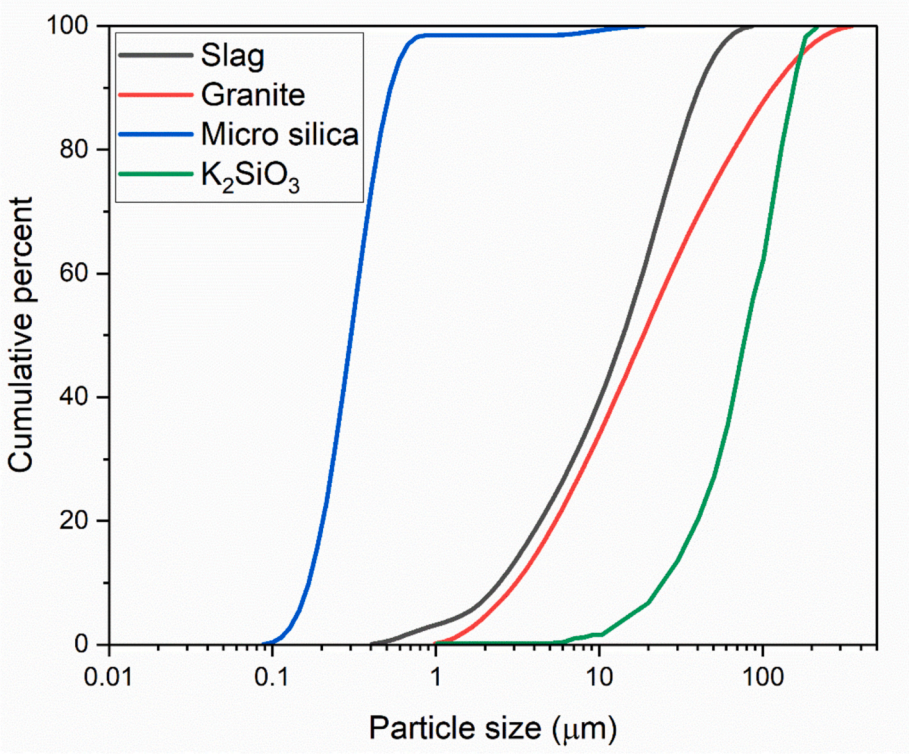

Fig. 1. Particle size distribution of the slag, granite, micro silica, K_2SiO_3 used in this study.

2.2.3. SEM analysis

The sample for the SEM measurement was prepared from the vacuum-dried samples, which were further impregnated with low-viscosity epoxy resin and then polished down to 0.25 μm (further details about the sample preparation can be found in [32]). Subsequently, the polished samples were analyzed using Philips XL30 with backscattering electron (BSE) mode at an acceleration voltage of 20 kV under low vacuum mode, with water vapor pressure kept at 1.0 Torr. A magnification of 1500× was used for the images. SEM analysis was done for the paste specimens after 0.5, 1, 3, 7, and 14 days. Thirty images were taken from every sample after each curing age.

The obtained SEM-BSE images were then used for image analysis using ImageJ [37]. In an SEM-BSE image, phases with a higher atomic number scatter more electrons so that they are brighter, while phases of lower atomic numbers absorb more electrons and are darker. The brightness of a pixel is represented by its grey value (with pixel values ranging from 0 (black) to 255 (white)) on the SEM-BSE image. The grey value is positively related to the backscattering coefficient, which is the fraction of scattered electrons. Different phases were segmented based on the threshold grey value that can be found from the grey value histogram, resulting in a binarized image (with a pixel value of either 0 (black) or 1 (white)) for each phase from each image. The segmented phases include pore, slag, potassium silicate, and granite and the reaction products. The potassium silicate and granite are considered as one phase because their grey values are very similar to each other. Thus, binarized images were then used to calculate the fraction of slag and reaction products. The volume fraction of the slag obtained from the image segmentation was used to calculate the degree of reaction of the slag ($\alpha_{slag}(t)$).

$$\alpha_{slag}(t) = \left(1 - \frac{VF_t}{VF_0}\right) \times 100\% \quad (2)$$

Here VF_t represents the volume fraction of slag at age t (from image segmentation) and VF_0 denotes the initial volume fraction of slag in the mix.

3. Numerical simulation model

Fig. 2 illustrates an overall flowchart of the numerical simulation framework GeoMicro3D. The GeoMicro3D model mainly consists of four components: 1) initial particle parking, 2) particle dissolution, 3) ion transport, and 4) nucleation and growth of reaction products. The simulation starts by building up an initial domain of the particles of the raw materials based on the mix design and particle size distributions. Further, the dissolution of different components (activator and precursor) in the alkaline environment is modeled in module 2. Following the dissolution step, the ions transport module is utilized to diffuse the ions in the microstructure of the paste. Lastly, the precipitation and growth of different reaction products in the microstructure of the paste are modeled in module 4. This dissolution-ions transport-nucleation-growth forms a simulation loop and is repeated until a target simulation time. More details about the implemented methodologies are stated in the following sections.

3.1. Determination of the initial simulation domain

In the first module, the initial simulation domain is built, which will undergo chemical reactions and microstructure formation. This involves the distribution of different solid particles, considering the particle size distribution (PSD) and shape of the particles. The Anm material model was used to simulate the initial spatial particle distribution of slag, K_2SiO_3, micro silica, granite [38–40]. According to the Anm model, the surface of the particle in the polar coordinate system ($r(\theta,\phi)$) can be expressed in terms of spherical harmonic coefficients (a_{nm}).

Table 3
Weight percentage of different components of the geopolymer paste.

Granite (%)	Slag (%)	Micro-silica (%)	K_2SiO_3 (%)	KOH (%)	Water (%)
29.1	28.3	2.6	12.71	2.59	24.8

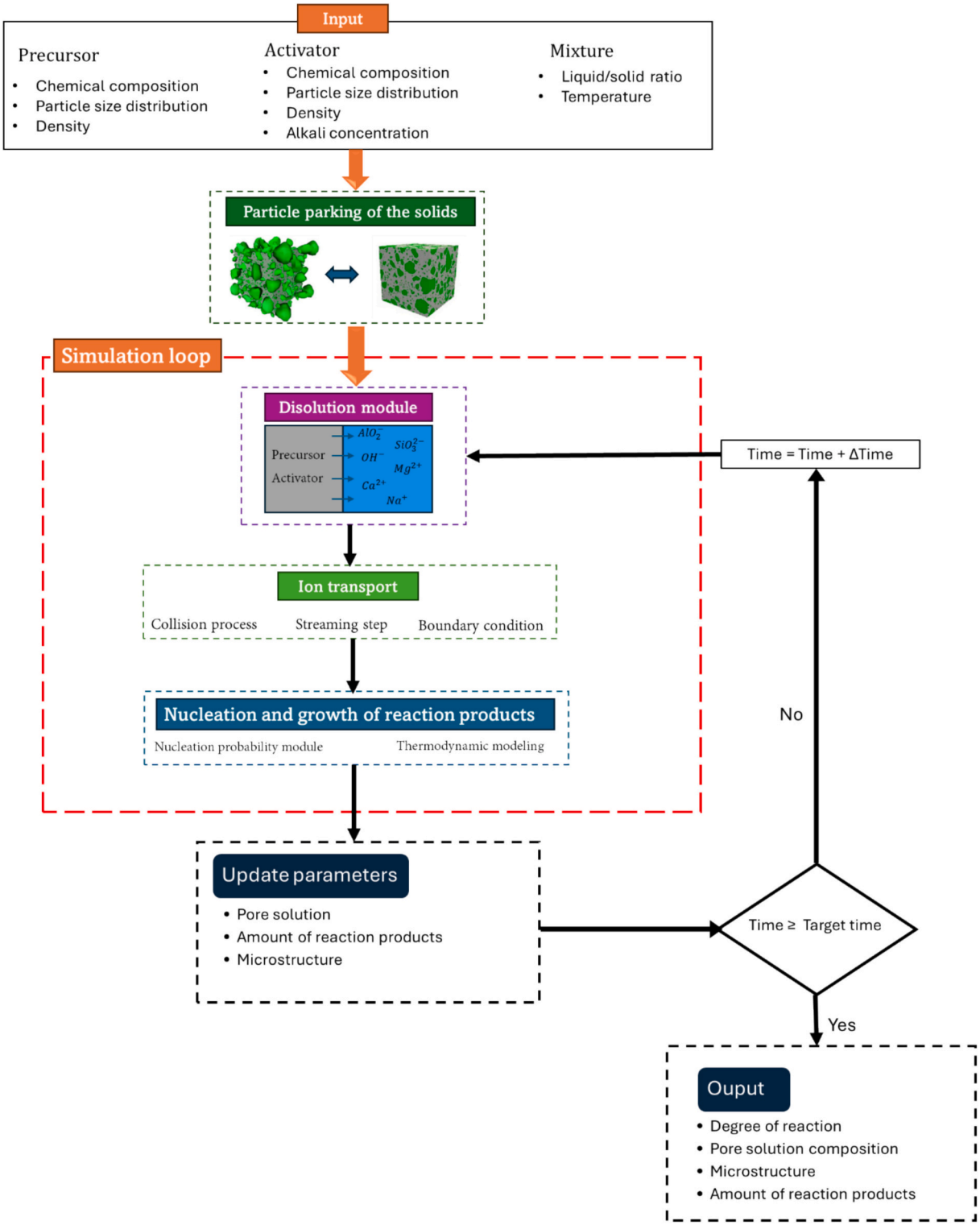

Fig. 2. The overall flowchart of the GeoMicro3D model.

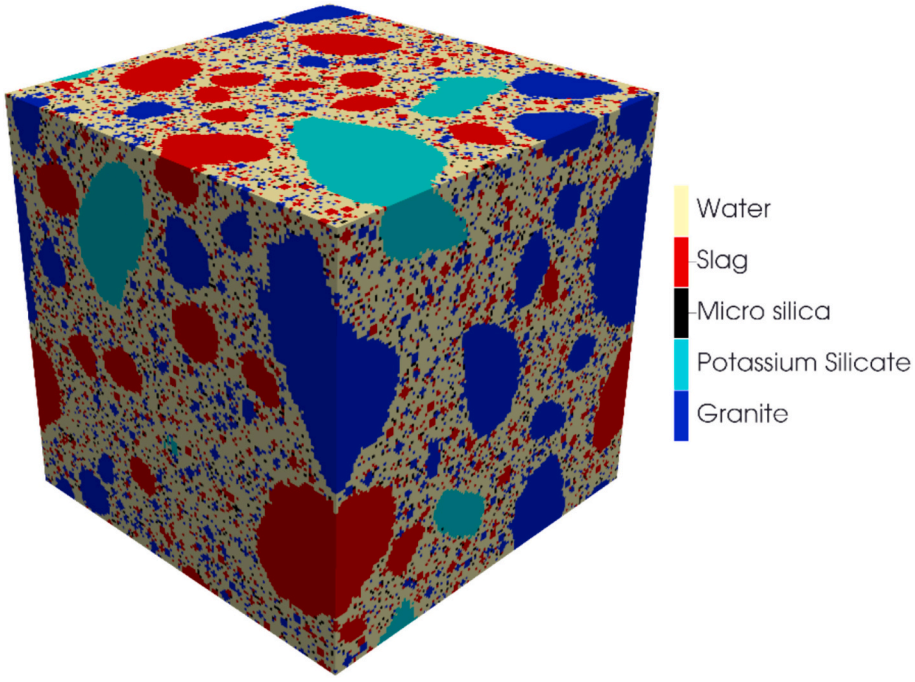

Fig. 3. Initial distribution of the different solids in the simulation domain.

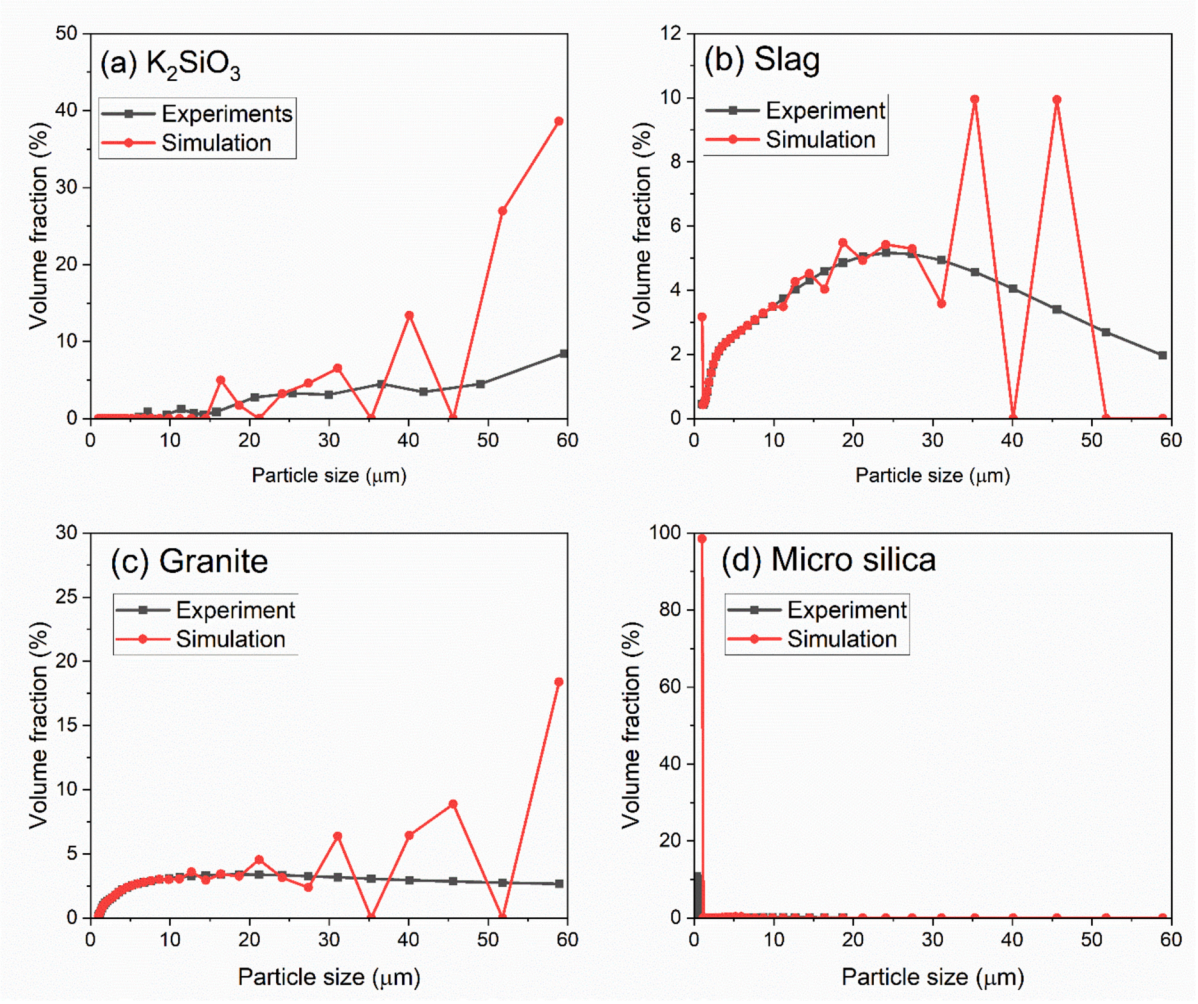

Fig. 4. Comparison of the simulated particle size distribution with the experiential data.

$$r(\theta,\phi) = \sum_{n=0}^{\infty}\sum_{m=-n}^{n} a_{nm} Y_{nm}(\theta,\phi) \tag{3}$$

$$Y_{nm}(\theta,\phi) = \sqrt{\frac{(2n+1)(n-m)!}{4\pi(n+m)!}} P_{nm}(cos\theta) e^{im\phi} \tag{4}$$

where:

- $r(\theta,\phi)$ – the radial distance from the particle center to the surface point.
- θ,ϕ – polar and azimuthal angle, respectively
- n,m – the indices ($-n \le m \le n$)
- $P_{nm}(cos\theta)$ – the associated Legendre polynomial
- i – the square root of -1 (i.e.$\sqrt{-1}$)

According to the literature [41], the size of the simulation domain should be at least 2.5 times bigger than the biggest particle size. Based on the particle size distribution (given in Fig. 1), the computation domain and cost will be high; thus, in order to maintain a balance, the particle size range between 1 and 60 μm is selected, with an overall domain size of 150 μm with a voxel size of 1 × 1 × 1 μm. The particle volume above 60 μm is then added to the particle at 60 μm, and the particle volume below 1 μm is added to the particles at 1 μm. Fig. 3 shows the initial distribution of the different solids (slag, granite, micro silica, and K_2SiO_3) in the simulation domain. X-ray computed micro-tomography can be used to measure the shape of the particles and compare them with the simulated microstructure.

Fig. 4 compares the particle size distribution of different solids obtained from the Anm model in the initial simulation domain with the experimental particle size distribution. It is apparent from Fig. 4, that at lower particle size, the simulated particle size in the domain matches well with the experimental PSD. However, some deviations from the experimental PSD can be observed at higher particle sizes. This is caused by the non-integer number of the calculated particle number during simulation, and the residual volume of the non-integer number is added to the volume of the particle at the next size. Hence, when the particle size is small, this discrepancy is not significant. In general, the simulated total solid volume and solid/liquid ratio match well with the experimental ones.

3.2. Particle dissolution

Once the solid particles come in contact with the pore solution, the dissolution starts. The dissolution of solids with different oxides is determined by the breaking of the bonds between oxygen and other elements. In the case of aluminosilicates such as slag, Si and Al build up the basic framework while some other alkali-earth element such as Ca, Mg, Na, and K modifies the framework. During dissolution in an alkali solution, these modifying elements are first released, followed by the breakdown of the Al—O bonds and then the Si—O bonds [42,43]. Thus, the dissolution of slag is represented by the dissolution of CaO, SiO_2, and Al_2O_3 in alkali solutions, as shown below.

$$CaO + H_2O \rightleftharpoons Ca^{+2} + 2OH^- \tag{5}$$

$$SiO_2 + 2OH^- \rightleftharpoons H_2O + SiO_3^{2-} \tag{6}$$

$$Al_2O_3 + 2OH^- \rightleftharpoons H_2O + 2AlO_2^- \tag{7}$$

The thermodynamic data of the above three reactions can be found in [44]. The dissolution rates of the above three reactions are modeled using the transition state theory [45,46]. According to this theory, the dissolution rate (r_χ) of any element χ can be written as:

$$r_\chi = r_\chi^+ \left(1 - \left(\frac{IAP_\chi}{Ksp_\chi}\right)^{1/\sigma}\right) \tag{8}$$

Where:

- r_χ – Overall dissolution rate (mol/m^{2}s).
- r_χ^+ – Forward dissolution rate (far from equilibrium dissolution rate (mol/m^{2}s)).
- IAP_χ – Ion activity product for the component χ
- Ksp_χ – Solubility product
- σ – Ratio of dissolution rate of the activated complex relative to the overall reaction rate

The solubility products (Ksp_χ) of SiO_2, Al_2O_3, and CaO for dissolution were taken as 1.23 × 10^2, 3.0 × 10^0 and 2.31 × 10^{-1}, respectively [47–49]. Forward dissolution rate (or far from equilibrium dissolution rate) for CaO, SiO_2, and Al_2O_3 were estimated from the dissolution test for different solids, as explained in the Section 2.2.1. The dissolution rate of other elements, such as Na, K, and Mg, was derived from the dissolution rate of CaO, considering the molar ratio between the element and Ca in slag. For example, the dissolution rate of Mg (r_{Mg}) is estimated from the dissolution rate of Ca (r_{Ca}) as:

$$r_{Mg} = \frac{\nu_{Mg}}{\nu_{Ca}} r_{Ca} \tag{9}$$

Here ν_{Ca} and ν_{Mg} denote the molar fraction of Ca and Mg in slag respectively. Similarly, the dissolution of Na and K is also related to the dissolution of Ca. Further details about the dissolution model and equations are detailed in [35,36]. The dissolution rates of Si from micro silica and K and Si from K_2SiO_3 were determined based on the same principle. KOH is assumed to be completely dissolved in the water from the start of the simulation. The concentration of the pore solution in the model from the start was set to contain 1.86 mol/L of KOH.

The forward dissolution rate of slag is dependent on three factors, i.e., pH of the solution, temperature, and ratio of the non-bridging oxygen atoms to oxygen atoms in tetragonal coordination, i.e., NBO/T, which considers the degree of distortion in the framework structure of aluminosilicate materials [35,36,50]. The parameter NBO/T is calculated considering the oxide molar fractions as given by the equation below:

$$NBO\Big/T = \frac{2\left[CaO + MgO + K_2O + 3f_{fe}Fe_2O_3 + 3f_{Al}Al_2O_3 - \left(1-f_{fe}\right)Fe_2O_3 - (1-f_{Al})Al_2O_3\right]}{SiO_2 + TiO_2 + 2\left(1-f_{fe}\right)Fe_2O_3 + 2(1-f_{Al})Al_2O_3} \tag{10}$$

where the oxides represent molar fractions in the aluminosilicate material and, f_{fe} and f_{Al} are parameters that specify the molar fractions of Fe_2O_3 and Al_2O_3 that act as framework modifiers and are taken as 0.15 in this study. The effects of pH and NBO/T on the dissolution rate were considered by deriving a relationship based on the particle dissolution tests (Section 2.2.1). The derivation of dissolution rate for different ions from different solids is detailed in Section 4.1. In the simulation, the voxels on the surface of the solid particles are allowed to dissolve to the nearest voxels. Thus, at a solid surface, voxels can dissolve to six near

voxels (one in each direction). Similarly, the ions at each voxel come in the solution from the six nearest solid voxels. The dissolved amount of ions at any voxel (ΔN_ψ) can be written by Eqs. (11) and (12).

$$\Delta n_{\psi,i} = f_{diss} r_{\psi,i} . t_0 l_0^2 \tag{11}$$

$$\Delta N_\psi = \sum_{i=1}^{6} \Delta n_{\psi,i} \tag{12}$$

The parameter f_{diss} represents the area fraction of the interface that is being dissolved. This parameter is taken as $(1 - V_f)^n$. V_f denotes the volume fraction of solids in the voxel; thus, if the voxel is completely filled with the solids, the dissolution of ions doesn't happen to that voxel. $\Delta n_{\psi,i}$ denotes the released amount of ion ψ on interface i. t_0, $r_{\psi,i}$ and l_0 represent the time step, the dissolution rate of the ion ψ on interface i and the side length of the voxel, respectively.

3.3. Ion transport

Following the dissolution step, the ion transport module is used to simulate the transport of the ions in the microstructure. The transport of ions during the hydration process is purely diffusive in nature. In this study, the Lattice Boltzmann method (LBM) with cubic lattice model D3Q7 is used to simulate the diffusion of ions. The multi-relaxation time approach allows the distribution functions in different directions to evolve at different relaxation rates and allows anisotropic diffusion of ions in the lattice [51–53]. The evolution equation of distribution functions $g_i = g_i(x,t)$ by LBM -MRT can be written as:

$$\begin{aligned} g_i(x + c_i\delta t, t + \delta t) = g_i(x,t) - \left(M^{-1} S_d M\right)_{ij} \left[g_j(x,t) - g_j^{eq}(x,t)\right] \\ + \delta t \left[M^{-1}\left(I - \frac{S_d}{2}\right) M\right]_{ij} S_j \end{aligned} \tag{13}$$

Where i and j are the diffusion directions $\forall\ i,j \in [0,6]$. c_i denotes the discrete velocity at x and time t, and can be written as $\delta x/\delta t$, where δx and δt represent the lattice spacing and time. $g_j^{eq}(x,t)$ denotes the equilibrium distribution function, which can be written as:

$$g_j^{eq}(x,t) = \omega_i C \tag{14}$$

where ω_i is the weight coefficient ($\omega_i = \frac{1}{7} \forall\ i \in [0,6]$), and C is the concentration of ions at any lattice node. I, M and S_d represent the identity matrix, transformation matrix, and diagonal relaxation matrix, respectively, which are given in Eqs. (15) and (16).

$$M = \begin{bmatrix} 1 & 1 & 1 & 1 & 1 & 1 & 1 \\ 0 & 1 & -1 & 0 & 0 & 0 & 0 \\ 0 & 0 & 0 & 1 & -1 & 0 & 0 \\ 0 & 0 & 0 & 0 & 0 & 1 & -1 \\ 6 & -1 & -1 & -1 & -1 & -1 & -1 \\ 0 & 2 & 2 & -1 & -1 & -1 & -1 \\ 0 & 0 & 0 & 1 & 1 & -1 & -1 \end{bmatrix} \tag{15}$$

$$S_d = \begin{bmatrix} s_0 & 0 & 0 & 0 & 0 & 0 & 0 \\ 0 & s_1 & 0 & 0 & 0 & 0 & 0 \\ 0 & 0 & s_1 & 0 & 0 & 0 & 0 \\ 0 & 0 & 0 & s_1 & 0 & 0 & 0 \\ 0 & 0 & 0 & 0 & s_2 & 0 & 0 \\ 0 & 0 & 0 & 0 & 0 & s_2 & 0 \\ 0 & 0 & 0 & 0 & 0 & 0 & s_2 \end{bmatrix} \tag{16}$$

Where s_i is the relaxation parameter for the i^{th} moment of the distribution function, such that $s_0 = 0$, $s_1 = 1/\tau$, and $s_2 = 1 - s_1$. τ is the relaxation time, which is related to the diffusion coefficient (D) (m^2/s) as:

$$D = \frac{1}{2}\left(\tau - \frac{1}{2}\right)\frac{\delta x^2}{\delta t} \tag{17}$$

S_j is the source term in the j^{th} direction, which can be expressed in terms of source term $\overline{S}$ (as)

$$S_j = \omega_i \overline{S} \tag{18}$$

The source term takes into account the amount of ions dissolved and consumed in the product formation at any step. The concentration of ions at any lattice node can be written as:

$$C(x,t) = \sum_{i=0}^{6} f_i(x,t) \tag{19}$$

SiO_3^{2-}, AlO_2^-, Ca^{2+}, Mg^{2+}, $K^+$and Na^+ are considered for diffusion in the current simulation, and their diffusion coefficients in water are taken from [54,55]. The primary amorphous reaction products (alkali calcium-aluminosilicate hydrate, C-(N, K-)A-S-H gel) and pore are diffusive for ions, while the precursors, the activator, and the secondary crystal reaction products (crystals) are considered non-diffusive. The relative diffusivity of the ions in the C-(N,*K*)-A-S-H gel is taken as 0.0025 [56]. For the lattice nodes with partial diffusion and non-diffusive components, the effective diffusion coefficient is calculated. The details of the effective diffusion coefficient can be found in [50]. The bounce-back condition is applied to completely non-diffusive lattice nodes. Periodic boundary conditions are implemented across the simulation domain's surface, ensuring ions diffusing out from the top surface re-enter from the bottom surface and vice versa. Likewise, the same principle applies to the back-front and left-right surfaces.

3.4. Nucleation and growth of reaction products

The concentration of the different ions in the solution increases due to the dissolution of precursors and activators. As a result, the pore solution becomes supersaturated with respect to different reaction products, and products start to nucleate in the microstructure of the paste. Nucleation of a product at any location starts to occur when the nuclei of a reaction product/s reach a critical size. The classical nucleation and growth theory is adopted in the model for the nucleation of products in the microstructure [57,58]. According to this theory, the probability $P(t)$ that one critical nucleus is formed in a time interval (Δt) can be given as:

$$P(\Delta t) = 1 - e^{(-J.V.\Delta t)} \tag{20}$$

Here V denotes the volume of the solution (in m^3) in which the nucleus is probable to form, and J represents the nucleation rate ($m^{-3}s^{-1}$), which depends on the supersaturation ratio (S) and can be written as:

$$J(S) = A.S.e^{\left(\frac{-B}{ln(S)}\right)} \tag{21}$$

Here A and B denotes the kinetic parameter and thermodynamic parameter of nucleation, respectively. The kinetic parameter (A) ($m^{-3}.s^{-1}$) for all the products is taken similarly to that of [35]. B parameter is expressed with the following equation:

$$B = \frac{4}{27}\frac{c^3 v^2 \gamma_{ef}^3}{k_B^3 T^3} \tag{22}$$

In the above equation, c is the shape factor (which is $36\pi^{1/3}$ for spheres and 6 for cubes), v is the molar volume of the reaction product (m^3), k_B is the Boltzmann constant ($J.K^{-1}$), T is the temperature (K), γ_{ef} is the effective interfacial energy such that $\gamma_{ef} = \psi\gamma$. ψ is the activity factor $0 < \psi < 1$. The interfacial energy γ is calculated using the following equation [35,50]:

$$\gamma = \beta_N . k_B . T . \left(\frac{1}{v^{2/3}}\right) . ln\left(\frac{1}{N_a v c^*}\right) \tag{23}$$

where β_N, N_a and c^* are numerical factors ($\beta_N = 0.514$ for spherical nuclei), Avogadro's number and molar solubility (mol/L), respectively.

Table 4
Dissociation reactions and solubility products (Log(K_{sp})) for C-(N, K)A-S-H and 25 °C and 1 bar.

Solids	Dissociation reactions	Log (K_{sp})
CNASH_ss model		
5CA	$(CaO)_{1.25}(Al_2O_3)_{0.125}(SiO_2)_1(H_2O)_{1.625} \rightleftharpoons 1.25Ca^{2+} + SiO_3^{2-} + 0.25AlO_2^- + OH^- + 1.5H_2O$	10.75
INFCA	$(CaO)_1(Al_2O_3)_{0.15625}(SiO_2)_{1.1875}(H_2O)_{1.65625} + 0.6875OH^- \rightleftharpoons Ca^{2+} + 1.1875SiO_3^{2-} + 0.3125AlO_2^- + 2H_2O$	8.90
5CNA	$(CaO)_{1.25}(Na_2O)_{0.25}(Al_2O_3)_{0.125}(SiO_2)_1(H_2O)_{1.375} \rightleftharpoons 1.25Ca^{2+} + SiO_3^{2-} + 0.25AlO_2^- + 0.5Na^+ + 0.75OH^- + H_2O$	10.40
INFCNA	$(CaO)_1(Na_2O)_{0.34375}(Al_2O_3)_{0.15625}(SiO_2)_{1.1875}(H_2O)_{1.3} \rightleftharpoons Ca^{2+} + 1.1875SiO_3^{2-} + 0.3125AlO_2^- + 0.6875Na^+ + 1.3125H_2O$	10.70
INFCN	$(CaO)_1(Na_2O)_{0.3125}(SiO_2)_{1.5}(H_2O)_{1.1875} \rightleftharpoons Ca^{2+} + 1.5SiO_3^{2-} + 0.625Na^+ + 1.375H_2O$	10.70
5CKA	$(CaO)_{1.25}(K_2O)_{0.25}(Al_2O_3)_{0.125}(SiO_2)_1(H_2O)_{1.375} \rightleftharpoons 1.25Ca^{2+} + SiO_3^{2-} + 0.25AlO_2^- + 0.5K^+ + 0.75OH^- + H_2O$	10.40
INFCKA	$(CaO)_1(K_2O)_{0.34375}(Al_2O_3)_{0.15625}(SiO_2)_{1.1875}(H_2O)_{1.3} \rightleftharpoons Ca^{2+} + 1.1875SiO_3^{2-} + 0.3125AlO_2^- + 0.6875K^+ + 1.3125H_2O$	10.70
INFCK	$(CaO)_1(K_2O)_{0.3125}(SiO_2)_{1.5}(H_2O)_{1.1875} \rightleftharpoons Ca^{2+} + 1.5SiO_3^{2-} + 0.625K^+ + 1.375H_2O$	10.70
T2C	$(CaO)_{1.5}(SiO_2)_1(H_2O)_{2.5} \rightleftharpoons 1.5Ca^{2+} + SiO_3^{2-} + OH^- + 2H_2O$	11.60
T5C	$(CaO)_{1.25}(SiO_2)_{1.25}(H_2O)_{2.5} \rightleftharpoons 1.25Ca^{2+} + 1.25SiO_3^{2-} + 2.5H_2O$	10.50
TobH	$(CaO)_1(SiO_2)_{1.5}(H_2O)_{2.5} + OH^- \rightleftharpoons Ca^{2+} + 1.5SiO_3^{2-} + 3.0H_2O$	7.90

Table 5
Thermodynamic data of all the reaction products at 25 °C and 1 bar.

Phase	V^0 (cm^3/mol)	$\Delta_f H^0$(kJ/mol)	$\Delta_f G^0$(kJ/mol)	S^0(J/mol.K)	C_p^0 (J/mol.K)
5CA	57.3	−2491	−2293	163	177
INFCA	59.3	−2551	−2343	154	181
5CNA	64.5	−2569	−2382	195	176
INFCNA	69.3	−2667	−2474	198	180
INFCN	71.1	−2642	−2452	186	184
5CKA	64.5	−2578	−2392	202	181
INFCKA	69.3	−2680	−2488	208	186
INFCK	71.3	−2654	2465	194	189
T2C	80.6	−2721	−2465	167	237
T5C	79.3	−2780	−2517	160	234
TobH	85.0	−2831	−2560	153	231
M_4AH_{10}	219.1	−7160	−6358	549	648
M_6AH_{12}	305.4	−9007	−8023	675	803
$M8AH_{14}$	392.3	−10,853	−9687	801	958
Natrolite	169.0	−5728	−5325	360	359
Nat (K)	186.6	−5738	−5344	416	370

In the current study, heterogeneous precipitation is allowed, which refers to the precipitation on the surface of the particle. The reaction products are mainly divided into two categories, i.e., primary products and secondary products. The primary reaction products include alkali calcium-aluminosilicate hydrate, C-(N, K-)A-S-H gel, while secondary products include crystal phases such as zeolites and hydrotalcite-like phases. Nucleation probability is calculated for each product at each lattice node. In the microstructure, the primary and secondary products are always mixed. Due to computation limitations, the precipitation cannot be allowed on all probable nodes. Thus, in the current model, the precipitation of reaction products at any nodes is allowed to happen when at least one of the end members of the C-(Na, K)-A-S-H gel and at least one of the secondary products are probable to precipitate. Further details of the nucleation modeling strategy can be found in [35,50].

After the nucleation step, thermodynamic modeling is used to estimate the amount and type of the reaction products to be precipitated at any node. The primary reaction product in the case of alkali-activated slag is C- (N, K)-A-S-H gel. The structure and composition of C- (N, K)-A-S-H depends on the type of activator and slag. In this study, the CNASH_ss model was used to represent the C-(Na, K)-A-S-H gel in the system [59]. In this work, potassium silicate is used as an activator instead of sodium silicate. The thermodynamic data for C-K-A-S-H is not available in the literature. However, literature [60] suggests that the role of the ionic radius of the activator in determining the products in an alkali activator system is very minor. Further, some studies [61,62] suggest that (Na + K)/(Al + Si) ratios of the C-(Na, K)-A-S-H products are independent of the nature of the alkali element. Both Na and K are incorporated into the interlayer spaces of the C-(Na, K)-A-S-H gel. Thus, CNASH_ss is used in this study, with additional end members added to replace sodium with potassium. In addition to the primary products, secondary products were also included in the modeling. This includes hydrotalcite-like phases, which are modeled using the MA-OH-LDH_ss model [63–65]. Sodium and potassium zeolites (Natrolite and Nat(K) respectively) were also included in the model using the thermodynamic model Zeolites21 [66,67]. Dissociation reactions and solubility products for C-(Na, K)-A-S-H gel are shown in Table 4, and thermodynamic data for different products used in the model are given in Table 5.

Thermodynamic calculations have been performed using the thermodynamic modeling platform GEMS-selector V3 [68,69]. The thermodynamic database used in the model includes the CEMDATA18 database reported in [44], zeolites21 databases as reported in [66,67], and CNASH_ss and MA-OH-LDH_ss databases as mentioned in [59,63]. The ion activity coefficients in the GEM- Selector employed the extended Debye-Huckle equation [68,69]:

$$log_{10}\left(\gamma_j\right) = \frac{-A_\gamma z_j^2\sqrt{I}}{1+\dot{a}B_\gamma\sqrt{I}} + b_\gamma I + log_{10}\left(\frac{x_{jw}}{X_w}\right) \quad (24)$$

Where:

- γ_j - the activity coefficient
- z_j - charge of the ions
- j - the aqueous species
- A_γ, B_γ - the electrostatic parameters
- I - the ionic strength
- x_{jw} - the mole quantity of water
- X_w - the total mole amount of the aqueous phase
- $\dot{a}$ - the average ion size
- b_γ - the parameter for common short-range interactions of the charged species

After calculating the reaction products, they are assumed to be deposited in the voxel until the voxel is completely filled. The CNASH_ss model only takes into account the interlayer water. In GeoMicro3D, the absorbed and gel water is also considered. 0.3 mol of water, with a density of 1.1 g/cm^3, is added to account for the adsorbed water. For gel water in CNASH gel, additional water is added so that the H_2O /SiO_2 ratio is maintained at 4. The density of the gel water is taken as 1.0 g/cm^3 [35].

Table 6
Diffusion coefficient and activation energy of different ions at 25 °C.

Ions	SiO_3^{2-}	AlO_2^-	Ca^{2+}	Mg^{2+}	K^+	Na^+
D_{ref} (m^2/s)	0.7×10^{-9}	0.6×10^{-9}	0.72×10^{-9}	0.71×10^{-9}	1.96×10^{-9}	1.33×10^{-9}
E_{diff} (J/mol)	2.46×10^4	2.04×10^4	2.32×10^4	1.26×10^4	1.60×10^4	1.67×10^4

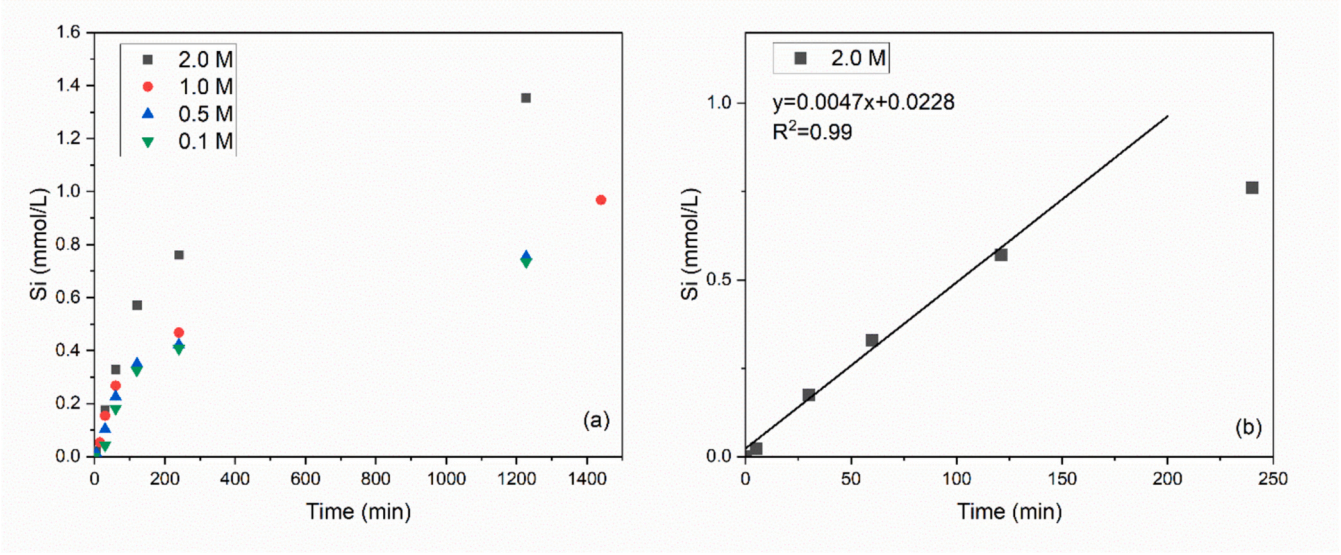

Fig. 5. (a) Measured Si ion concentration at different alkali concentrations (b) slope of the linear fitting of the Si ion concentrations at 2.0 M alkali concentration.

3.5. Effect of temperature

The effect of temperature is considered on the forward dissolution rate and the diffusion coefficient of the ions using the Arrhenius equation. The forward dissolution rate refers to the rate that operates at a very low degree of saturation (far from equilibrium), and the Arrhenius equation can be applied to consider the effect of temperature [70–72]. The equations can be written as:

$$r_{\chi,T} = r_{\chi,ref}.exp\left[\frac{E_a}{R}\left(\frac{1}{T_{ref}}-\frac{1}{T}\right)\right] \quad (25)$$

$$D_T = D_{ref}.exp\left[\frac{E_{diff}}{R}\left(\frac{1}{T_{ref}}-\frac{1}{T}\right)\right] \quad (26)$$

Where

- $r_{\chi,T}$ – the new forward dissolution rate at temperature T (in Kelvin)
- $r_{\chi,ref}$ – Forward dissolution rate at a reference temperature T_{ref} (in Kelvin)
- D_T – the new diffusion coefficient (m^2/s) at temperature T
- D_{ref} – diffusion coefficient at reference (m^2/s) temperature T_{ref}
- R – the universal gas constant
- E_a – the activation energy for the dissolution (J/mol)
- E_{diff} – the activation energy of diffusion (J/mol)

The activation energy (E_a) of SiO_2, Al_2O_3 and CaO were taken as 8.3 × 10^4 J/mol, 8.0 × 10^4 J/mol and 1.36 × 10^4 J/mol respectively [47–49]. The diffusion coefficient for all the ions and corresponding activation energy are given in Table 6 [54,55]:

3.6. Effect of solution-volume to surface-area ratio

The dissolution of the solids depend on the particle size distribution and the resolution of the simulation. To reduce the effect of differences in the particle size distribution between the experiment and modeling, the effect of solution-volume to slag-surface-area ratio is considered. Let the change in the element concentration in experiment (ΔC_{exp}) and numerical simulation (ΔC_{model}) due to dissolution are given by the equations below:

$$\Delta C_{exp} = \frac{r_{x+,exp} \times S_{exp} \times dt}{V_{exp}} \quad (27)$$

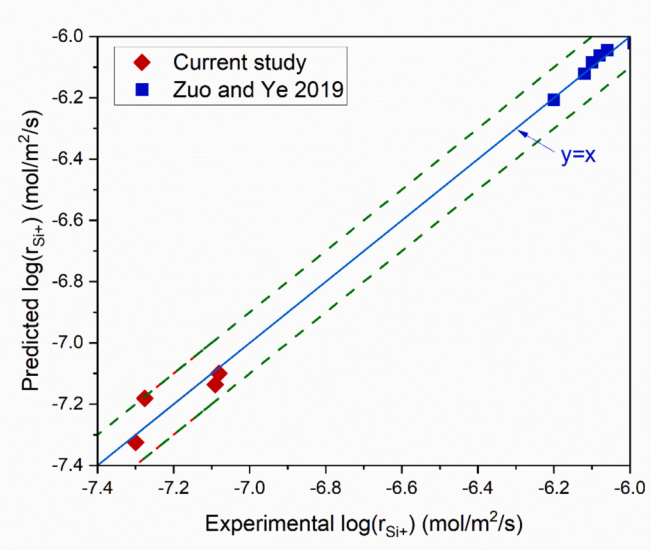

Fig. 6. Predicted log forward dissolution of Si compared with the experimental results.

$$\Delta C_{model} = \frac{r_{x+,model} \times S_{model} \times dt}{V_{model}} \quad (28)$$

where ΔC r_{x+}, S and V represent element concentration (mol/m^3) change over time dt (s), forward dissolution rate ($mol/m^2/s$), solid surface area (m^2/kg) and solution volume (m^3), respectively, in experiment and numerical simulation. In order to consider the effect of differences in particle size and resolution of the computation domain, the change in concentration from experiment and simulation should be same i.e.

$$\Delta C_{model} = \Delta C_{exp} \quad (29)$$

Further solving the above equation gives:

$$r_{x+,model} = \left(\frac{V_{model}/S_{model}}{V_{exp}/S_{exp}}\right) r_{x+,exp} \quad (30)$$

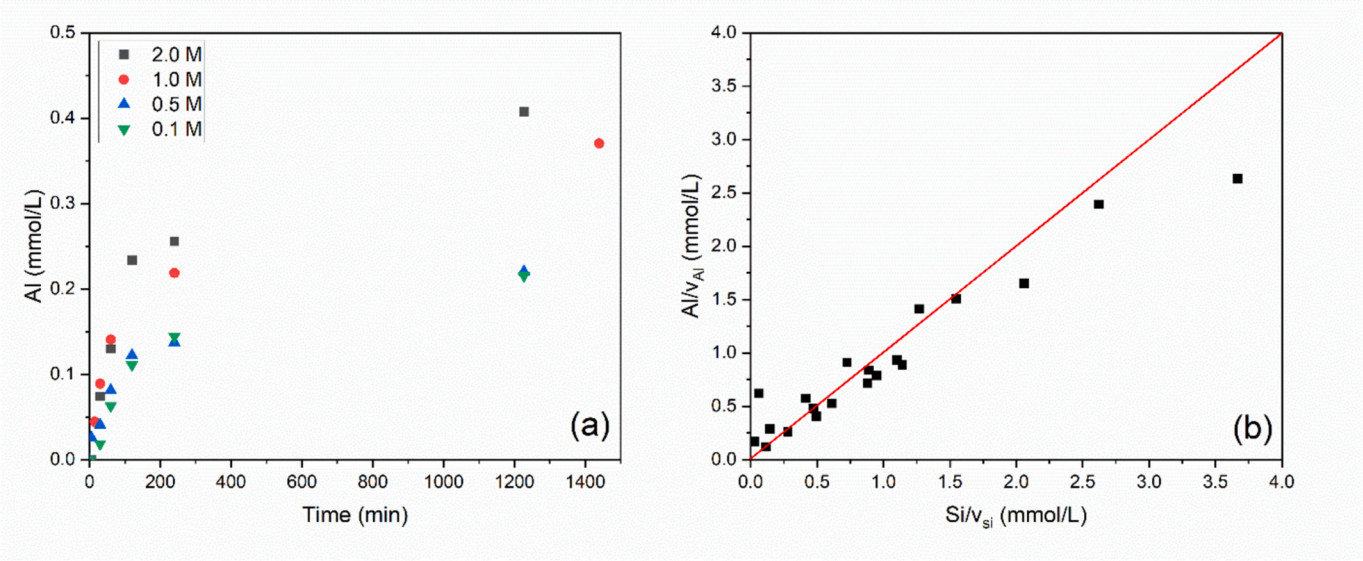

Fig. 7. (a) Measured Al ion concentration at different alkali concentrations (b) Al concentrations in solution normalized by the molar fraction of Al in the slag plotted against normalized Si concentration.

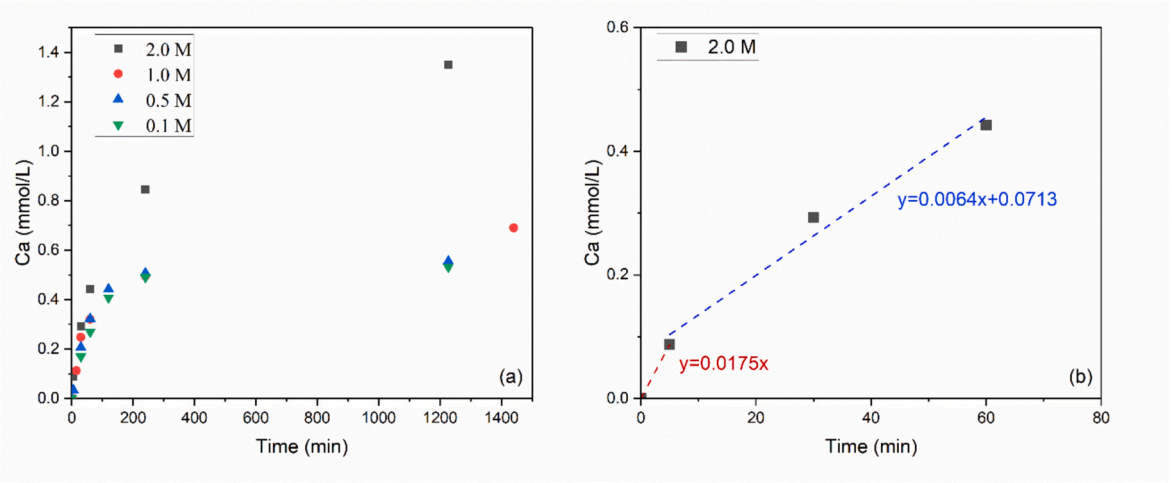

Fig. 8. (a) Measured Ca ion concentration at different alkali concentrations (b) slope of bilinear fitting for Ca ion concentrations at 2.0 M alkali concentration.

The dissolution rate thus calculated is used in the simulation, which accounts for the difference solution-volume/solid-surface-area ratio.

4. Results and discussion

4.1. Particle dissolution and dissolution rate calculation

This section first presents the experimental results for the dissolution of various ions (Ca, Si, and Al) from precursors and activators and the calculations for the forward dissolution rates of these ions. Finally, it compares the experimentally determined ion concentrations with the simulation data based on the calculated forward dissolution rates.

4.1.1. Dissolution of slag

Fig. 5 plots the Si ion concentration dissolved from slag with time at different alkali concentrations. It is apparent that higher Si ions are released in the solution at higher alkali concentrations. The dissolution of Si is initially linear with time. However, due to the precipitation of products, the dissolution becomes nonlinear (after 2 h). Thus, the forward dissolution rate is estimated using the slope of the linear fit line for the Si ion concentration in the first 2 h (as shown in Fig. 5(b) for an alkali concentration of 2.0 M).

The estimated forward dissolution rate is linked to the *pH* of the solution and the ratio of the non-bridging oxygen atoms to oxygen atoms in tetragonal coordination, i.e. *NBO*/*T*. Zuo and Ye [35,36,50] also conducted dissolution experiments for the slag at different alkali concentrations. Hence both data were used to derive the relation between the r_{Si+}, *NBO*/*T* and *pH* using the nonlinear curve fitting. The relationship is given below:

$$log_{10}r_{Si+} = -0.1934pH^{*}\frac{NBO}{T} + 0.5981pH + 6.4288^{*}\frac{NBO}{T} - 23.381 \quad (31)$$

Fig. 6 plots the predicted forward dissolution rate of Si with the experimental results. It is evident that the predicted results align well with the experimentally measured results within ±0.1 order magnitude.

Fig. 7 (a) plots the dissolution of Al from the slag with time at different alkali concentrations. The dissolution of Al from the slag is taken to be stoichiometric to Si in the slag [42,50]. According to the stoichiometric overall dissolution of Al and Si in from slag at the far-

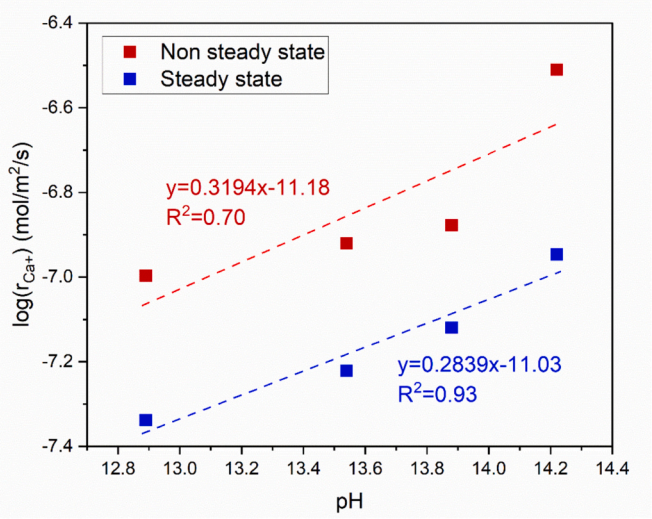

Fig. 9. Log forward dissolution of Ca (steady and non-steady state) plotted as a function of the pH of the solution.

from-equilibrium conditions, the log forward dissolution rates of Si and Al can be correlated as follows:

$$log_{10}r_{Al+} = log_{10}\left(\frac{\nu_{Al}}{\nu_{Si}}\right) + log_{10}r_{Si+} \quad (32)$$

ν_{Al} and ν_{Al} denote the molar fractions of Si and Al in the slag, respectively. Fig. 7 (b) plots the normalized concentration of the Al (Al concentration in solution divided by the molar fraction of Al in slag (ν_{Al})) with the normalized concentration of Si. The linear relationship in plot Fig. 7 (b) clearly indicates the stoichiometric dissolution of Al and Si from the slag.

The dissolution characteristics of Si and Al are different elements from Ca, Mg, Na, and K, as the former ones form the basic framework of the calcium aluminosilicate glasses (slag), while the latter modifies the framework [42,43]. The dissolution of Si and Al proceeds in a single steady state, which is also reflected in Fig. 5(b). The dissolution of Ca (cations) from the glasses proceeds in two stages: non-steady and steady-state. In the non-steady state, the release of the cations is governed by ion exchange, where selective leaching of alkali ions occurs, and Ca ions in the glasses are replaced by the H^+ from the solution. Following the non-steady stage is the network hydrolysis, when the steady dissolution of Ca occurs in the solution [73,74]. Hence, in the current study, the dissolution of Al is related to Si, while the dissolution of Mg, Na, and K is related to the dissolution of Ca.

Fig. 8 (a) plots the Ca ion concentration in the solution at different alkali concentrations, which also illustrates the two stages of Ca ion dissolution. The first linear curve in Fig. 8 (b) represents the non-steady stage, while the second linear curve denotes the steady stage. The slope of the line in two stages was used to calculate the dissolution rate using Eq. (1). The dissolution rate in the initial non-steady state is higher compared to the steady state. The dissolution rate is thus calculated for the two stages and is plotted against pH in Fig. 9. A linear relationship exists between the log forward dissolution rate for both stages and pH. Thus, the forward dissolution rate can be written as follows:

For non-steady state:

$$log(r_{Ca+}) = 0.3194pH - 11.18 \quad (33)$$

For steady state:

$$log(r_{Ca+}) = 0.2839pH - 11.03 \quad (34)$$

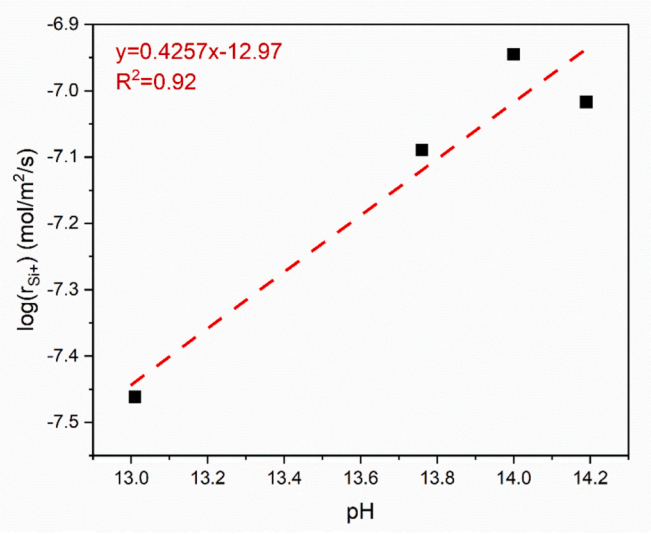

Fig. 11. Forward dissolution rate of Si from K_2SiO_3 in the first state with pH.

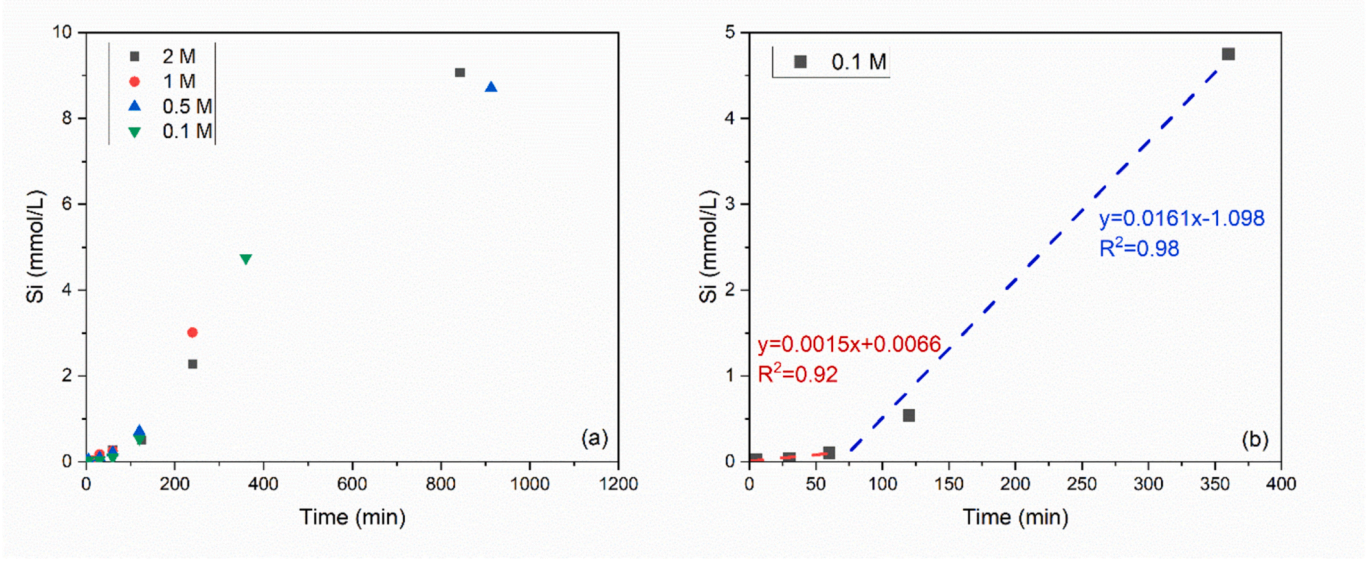

Fig. 10. Measured Si ion concentration for K_2SiO_3 different alkali concentration (b) slopes of bilinear fitting for Si ion concentration at 0.1 M alkali concentration.

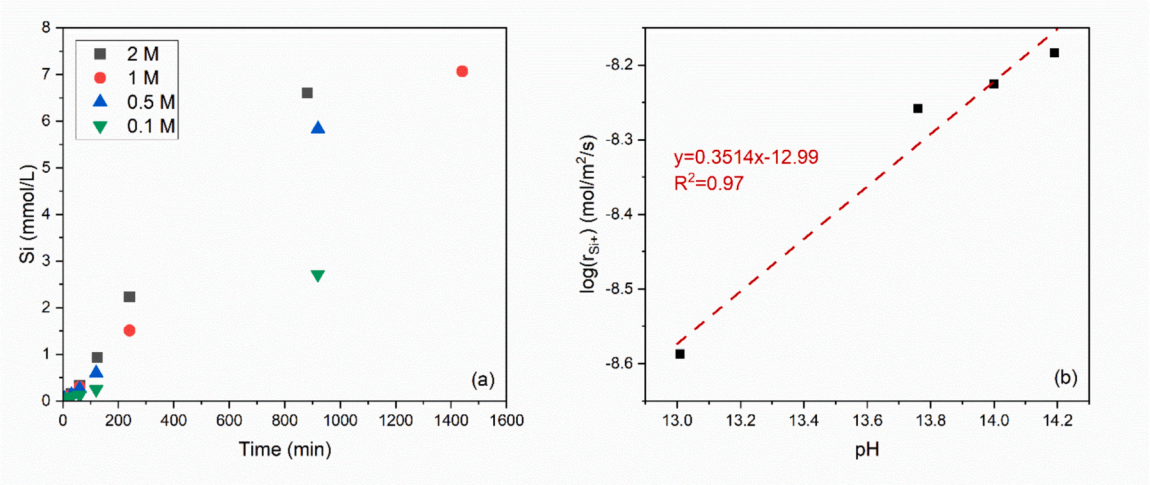

Fig. 12. (a) Measured Si ion concentration for micro silica at different alkali concentrations (b) forward dissolution rate of Si from micro silica with pH.

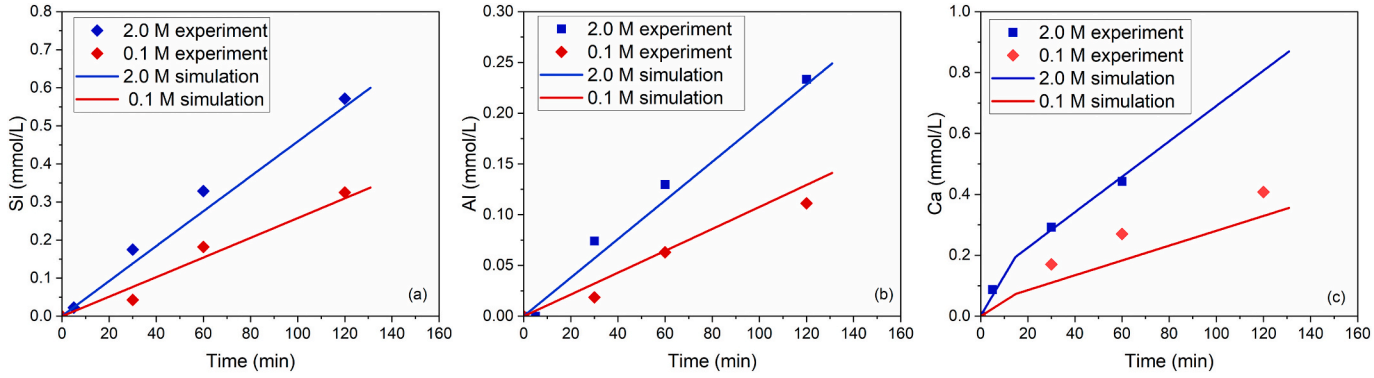

Fig. 13. Simulated concentration of different ions from slag compared with the experimental results (a) Si ions, (b) Al ions, and (c) Ca ions.

The effective saturation index (ESI) for the $Ca(OH)_2$ was calculated at different KOH concentrations to estimate the possibility of its formation in the solution, with ion activity coefficients calculated using the extended Debye-Huckle equation. ESI for $Ca(OH)_2$ at 0.1, 0.5, 1.0, and 2.0 mol/L was calculated to be −0.2, 0.6, 1.0, and 1.6, respectively. ESI values just above 0 indicate there is a low probability of the formation of $Ca(OH)_2$ in the solution. Zuo and Ye [36] also estimated ESI for different products under similar experimental conditions, and values were estimated to be negative or near zero. This ensured there was very small probability of precipitation of products in the solution.

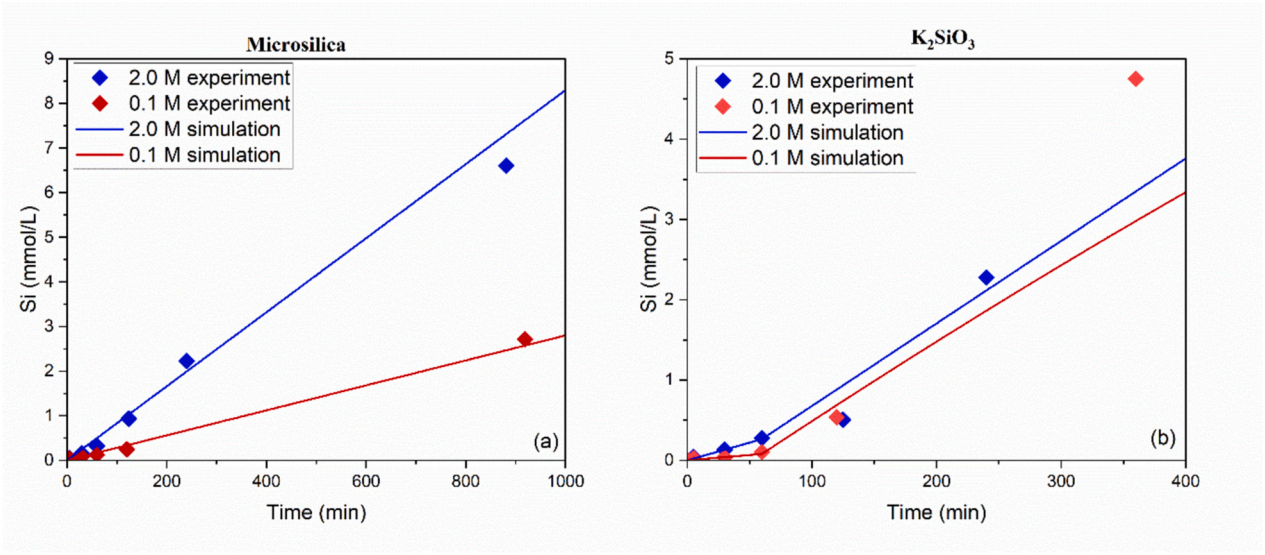

Fig. 14. Simulated and experimental concentration of Si ions dissolved from the raw materials (a) micro silica (b) K_2SiO_3.

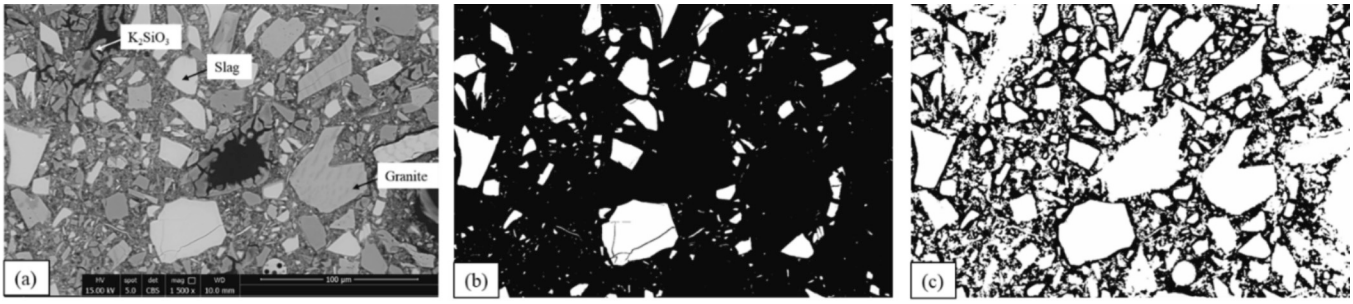

Fig. 15. (a) SEM BSE image after 7 days of curing, (b) segmented image of the geopolymer with white representing the slag, (c) segmented image with black representing the reaction products.

4.1.2. Dissolution of K_2SiO_3

For K_2SiO_3, the dissolution of Si ions is measured at different times in a solution with different alkali concentrations, and the dissolution of K is assumed to be based on the stoichiometry of the K_2SiO_3. Fig. 10(a) plots the Si ion concentration with time for different alkali concentrations. It is visible that the dissolution of Si from K_2SiO_3 shows two stages of dissolution rate. In the first stage, the dissolution is lower, and after 1 h, the dissolution rate reaches a steady stage (as shown in Fig. 10 (b)).

The forward dissolution rate in the first stage is found to be linearly related to the pH (as shown in Fig. 11), while the forward dissolution rate in the second stage is found to be independent of the pH. The relationship between pH and dissolution rate in the first stage can be written as:

$$log(r_{Si+}) = 0.4257pH - 12.97 \quad (35)$$

The dissolution rate in the steady state was calculated as follows:

$$log(r_{Si+}) = -6.6 \quad (36)$$

Notably, due to the longer dissolution time for K_2SiO_3, the larger particle could break into smaller particles, increasing the SSA and affecting the measured dissolution rate. Increasing the number of measurements during the early stages of dissolution could enhance the accuracy of the slope estimation and, consequently, the dissolution rate. It must be noted that, Eqs.(35) and (36) could change depending on the composition and structure of K_2SiO_3.

4.1.3. Dissolution of Micro silica

Fig. 12(a) plots the Si ion concentration dissolved from micro silica at different alkaline concentrations. The forward dissolution rate is estimated using the slope of the linear fit of the concentration and time plot. The forward dissolution rates thus estimated are found to be correlated to the pH (as shown in Fig. 12(b)). A linear relation is derived to relate the forward dissolution rates with the pH as given below:

$$log(r_{Si+}) = 0.3514pH - 12.99 \quad (37)$$

4.1.4. Comparison of the ion dissolution between experiments and model

This section compares the simulation output with the experimental values for the dissolution of different solids. Dissolution of different ions (Ca, Si, and/or Al) from slag, micro silica, and K_2SiO_3 were simulated at 2.0 M and 0.1 M concentrations of KOH using the simulation framework described in Section 3. Dissolution of the particles is simulated using the random particle shape for different raw materials using the forward dissolution rates estimated in Section 4.1 and using the Eq. (8). The chemical composition of different raw materials was used, as given in Table 1. For the simulation, the concentration of ions is measured at all the liquid voxels, and the average is taken.

Fig. 13 plots both simulated and experimental concentrations for the dissolution of slag (Si, Al, and Ca) at 2.0 M and 0.1 M of potassium hydroxide solution. It is evident that the simulated ion concentrations for Si, Al, and Ca are in good agreement with the experimental ion concentrations. The simulation can also capture the non-steady and steady-state dissolution of Ca from slag. Overall, the numerical model could simulate the dissolution of different ions from slag with reasonable accuracy.

Simulations were also carried out to check the dissolution of Si ions

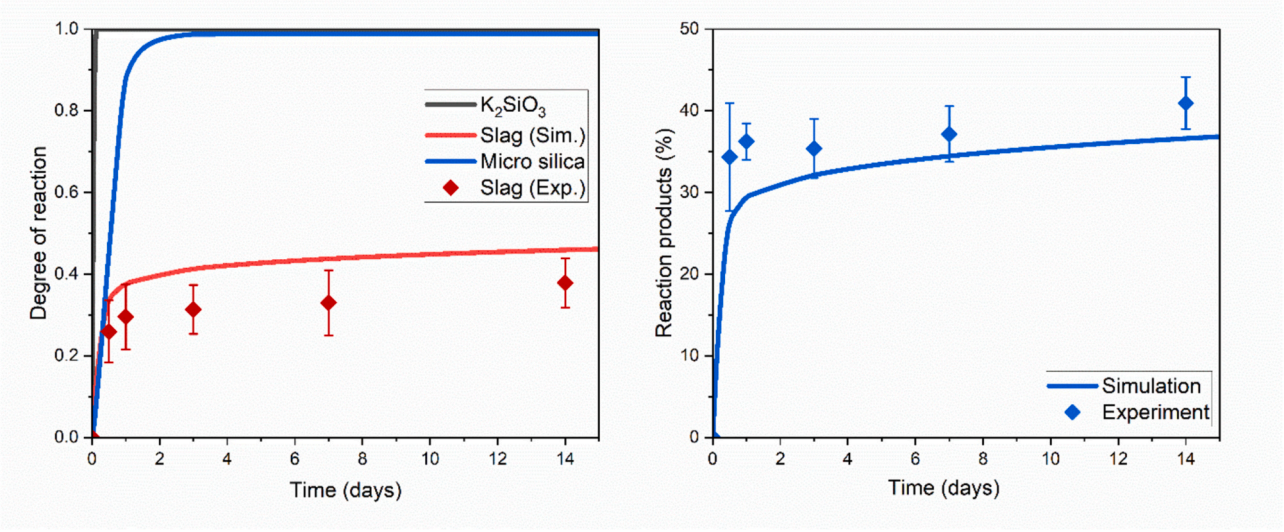

Fig. 16. (a) Comparison between the experimental and simulated degree of reaction, (b) comparison of the amount of reaction products from experiments and simulation.

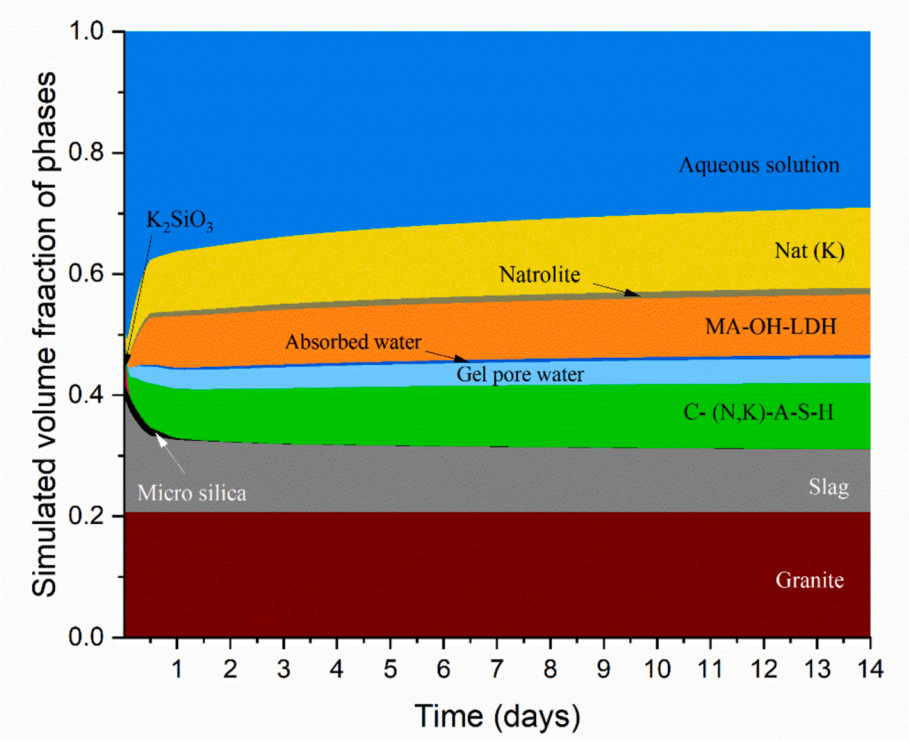

Fig. 17. Simulated volume proportion of phases with GeoMicro3D.

from micro silica and K_2SiO_3 at 2.0 M and 0.1 M concentrations of potassium hydroxide solution. Fig. 14 (a) and (b) plot the Si ion concentration in the solution from the experiments and its comparison with the simulation for the micro silica and K_2SiO_3 respectively. It is apparent that the simulation data aligns well with the experimental data for the micro silica, although some inconsistencies can be observed with the dissolution of K_2SiO_3. However, overall, all the simulation results show reasonable agreement with the experimental data.

4.2. *Microstructure development and pore solution of paste*

This section discusses the experimental data for the microstructure development obtained using SEM, the pore solution of the one-part granite-based geopolymer paste, and its comparison with the

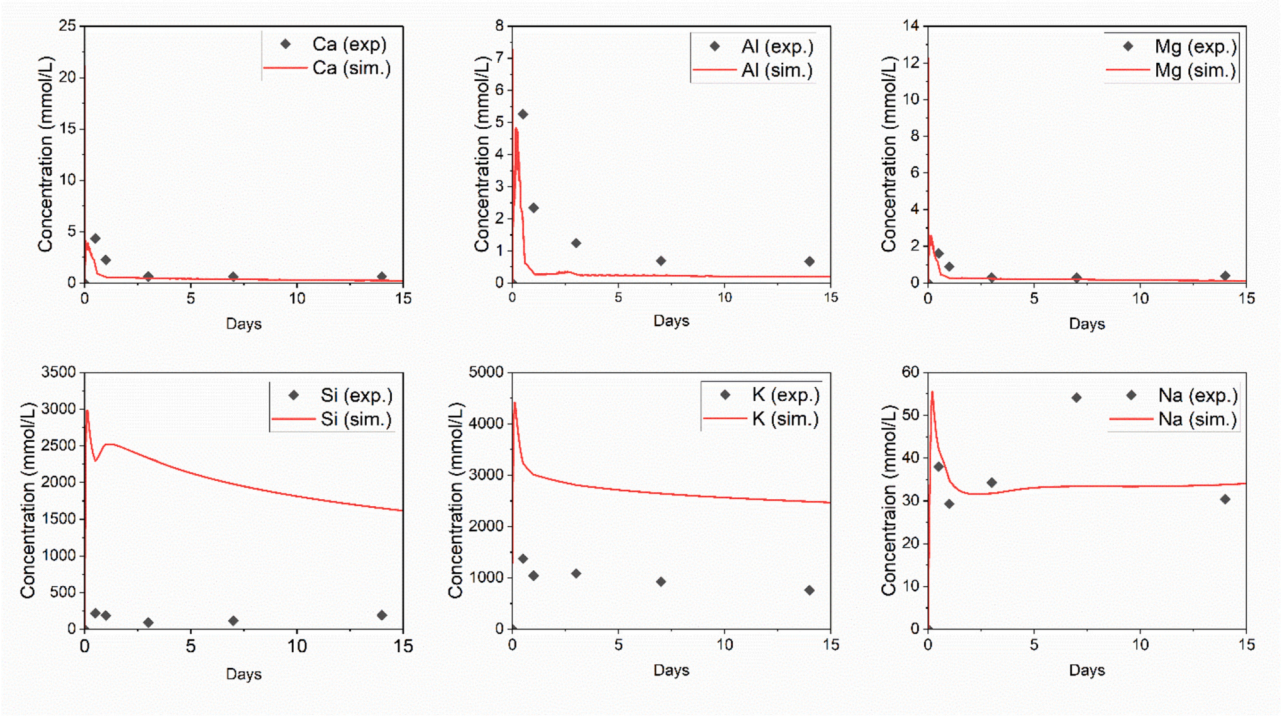

Fig. 18. Comparison of experimental and simulated concentrations of different ions in the pore solution.

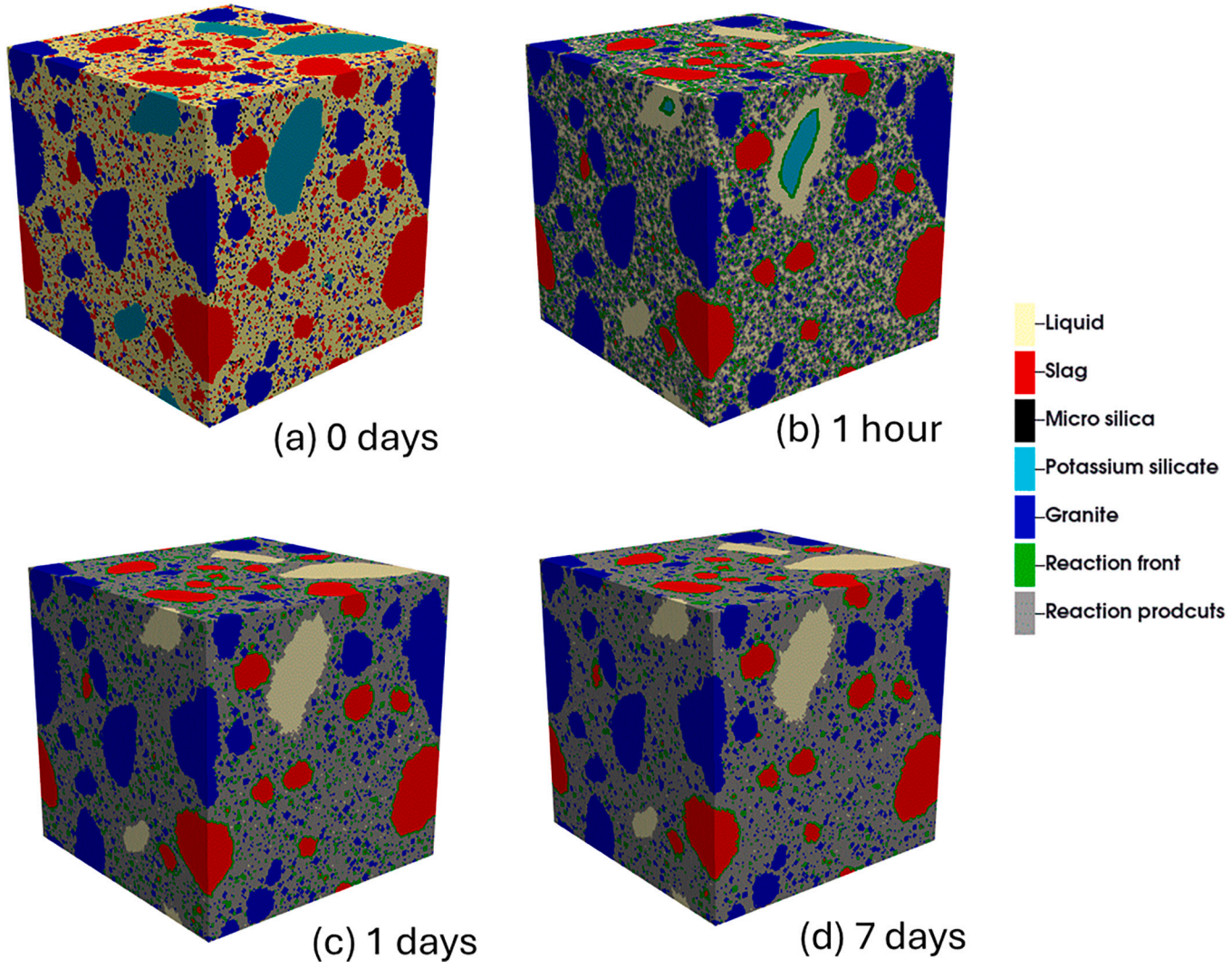

Fig. 19. Simulated microstructure of the one-part granite-based geopolymer after 0 days, 1 h, 1 day, and 7 days of curing.

modeling results.

Fig. 15 (a) shows the SEM-BSE image for the geopolymer after 7 days of curing. In the SEM images, the brighter phases correspond to the unreacted precursors, while the darkest phases correspond to the pores. The microstructure reveals a heterogeneous distribution of slag, granite, K_2SiO_3, and reaction products. It can be observed that the K_2SiO_3 has dissolved significantly, resulting in pores. Fig. 15 (b) shows the segmented image with white pixels representing the slag, which is used to estimate the degree of reaction of slag using Eq. (2). Fig. 15 (c) also shows the segmented image with black pixels corresponding to the reaction products. Fig. 16 (a) plots the degree of reaction (DOR) of slag obtained from the image segmentation and using Eq. (2) along with the simulated DOR for all the solids in the geopolymer. The DOR of slag increases rapidly in the first 12 h and reaches approximately 26%, and then it saturates. The DOR for slag reached around 40% after 336 h (14 days).

The numerical simulation for the one-part geopolymer is performed using the input microstructure (as shown in Fig. 3) and as the discussed methodology in Section 3. The dissolution rates for different raw materials are used as derived in Section 4.1. The dissolution of K_2SiO_3 was observed to be slow considering the non-steady and steady-state dissolution stage. Hence, only steady-stage dissolution was considered for the simulation of the paste. The simulation is carried out for 14 days of curing time at 20 °C. The DOR from the simulation is estimated by using the number of voxels of slag at any time (N_t) and the initial number of voxels (N_0) as given below:

$$\alpha_{slag}(t) = \left(1 - \frac{N_t}{N_0}\right) \tag{38}$$

It is apparent that the simulated DOR for slag is in good agreement with the experimental data. The model can capture the initial rise in the DOR (up to 12 h), and further then, the curve gets saturated with time. The DOR for slag estimated from the model reaches 0.46 after 14 days. The simulation shows that potassium silicate and micro silica dissolve completely in the solution. The potassium silicate is the activator, and due to the very fine size of micro silica, both reach complete hydration. The close alignment between the experimental data and model predictions for slag indicates that the model effectively captures the kinetics of the polymerization process.

Fig. 16 (b) plots the amount of reaction products obtained from the image segmentation along with the volume fraction of total reaction products from the simulation. The amount of reaction products (from the experiments) also shows a similar trend as the DOR for slag. Notably, the amount of reaction products obtained from the experiments also includes the pores, which are smaller than the resolution of the SEM-BSE images. The total reaction products calculated from the simulation include the gel water and absorbed water, as discussed in Section 3.4. For the simulation, it is evident that the amount of reaction products

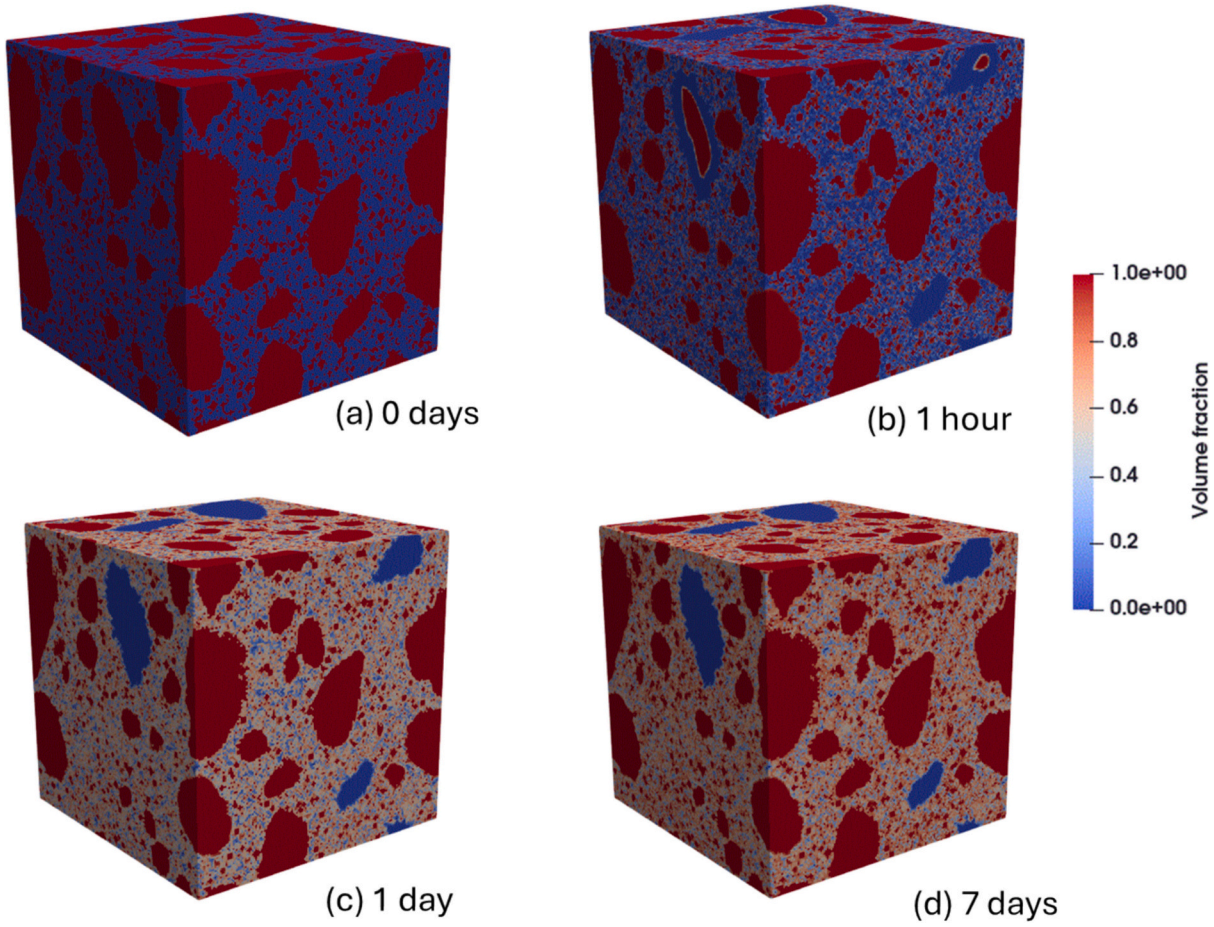

Fig. 20. Spatial distribution of the volume fraction of all phases in the microstructure of the paste after 0 days, 1 h, one day, and 7 days of curing.

increases in a similar trend as the degree of reaction for the slag, which includes an initial rapid increase in the reaction products up to 12 h and a plateau afterward. The agreement between the experimental and simulated amount of reaction products reinforces the reliability of the model and its applicability to predict product formation over time.

Fig. 17 illustrates the simulated volume fractions of various phases in the one-part granite-based geopolymer system over a 14-day period, as estimated using the GeoMicro3D. The main reaction products formed during hydration are C-(N, K)-A-S-H, MA-OH-LDH, and NAT (K). Natrolite is also formed in small quantities due to the release of Na ions from the slag. As the DOR of raw materials (slag, micro silica, and K_2SiO_3) increase rapidly in the early stage, the formation of C-(N, K)-A-S-H, MA-OH-LDH, and NAT (K) is also faster in the early stages, and further, it saturates with time.

Fig. 18 plots the concentration of Ca, Si, Al, Mg, Na, and K measured from the pore solution extracted from the paste using ICP-OES, along with the average ion concentrations in the voxels from the simulation. From the experimental data, it is apparent that the pore solution is mainly dominated by K and Si ions, as the former is released from the dissolution of the activator while the latter is released from K_2SiO_3, slag, and micro silica. The qualitative trends for Ca, Al, and Mg are very similar to each other, as the value is highest at 0.5 days due to the dissolution of slag, and then further it decreased with time due to ions being consumed in the precipitation of the products. The qualitative trends for elements are much similar, as discussed by [75].

From the simulated ion concentrations, it can be observed that all the curves first have an initial rise in concentration, which is due to the initial dissolution of ions from different solids in the pore solution. The concentration of ions keeps on increasing in the pore solution until the solution becomes supersaturated with respect to any of the reaction products mentioned in Table 5. Due to the supersaturation, the products start to precipitate, and the ions get consumed in the product formation, which decreases the ion concentration in the pores over time. It can be observed that a good agreement exists between the experimental and simulated data for Ca, Mg, Na, and Al. During the early ages of curing, the concentration of Ca and Mg (in the extracted pore solution) is higher relative to the solubility of $Ca(OH)_2$ and $Mg(OH)_2$. This suggests that the pore solution is oversaturated, and precipitation of products could occur in the pore solution. Due to the application of pressure to extract the pore solution, some metastable products could get dissolved due to chemo-mechanical effects increasing the concentration in the extracted pore solution [76,77]. Additionally, the passage of fine particles smaller than 0.45 μm could also contribute to minor changes in the measured concentrations [77].

The simulation results for the Si and K ions are overestimated. SEM-BSE images show some amount of unreacted K_2SiO_3. However, the model predicts complete hydration of K_2SiO_3, thus introducing a higher amount of K and Si ions in the system compared to the experiments. Additionally, in the current model, the Ca/Si ratio used for different products varies from 0.67 to 1.5, and the maximum Si/Al ratio for the zeolites was 1.5, which might be the reason for the overestimation of the Si ions in the system. Thus, for the low calcium system, the inclusion of more reaction products with low Ca/Si ratio and high Si/Al ratio could improve the model predictions.

Fig. 19 shows the simulated 3D microstructure development for the one-part geopolymer after 0 days, 1 h, 1 day, and 7 days. Yellow represents the voxels that are filled with the aqueous solution, grey represents the voxels partially or completely filled with the reaction products,

and green represents the reaction front. The reaction front represents the solid precursor and activator nodes, which are undergoing dissolution at any time. It is evident that after one hour, the K_2SiO_3 has dissolved significantly from the surface, and the size of the particles has reduced. It is also visible from Fig. 19 (c) that the finer particles of slag and micro silica have also dissolved after 1 day. The dissolution of potassium silicate has created some spaces in the microstructure, which is also observed from the SEM-BSE images, as shown in Fig. 15. In the current study, only heterogeneous precipitation is allowed, which refers to the precipitation on the surfaces. Due to the absence of any nucleation site in the spaces created due to the dissolution of K_2SiO_3, precipitation couldn't happen.

Fig. 20 shows the simulated 3D microstructure development of the paste after 0 days, 1 h, 1 day, and 7 days. Fig. 20 shows the volume fraction at different voxels (this includes precursor, activator, and reaction products). The dissolution of the precursors and activator and precipitation of the reaction products are clearly visible. The products are precipitating on the surface of all the particles and microstructure is becoming denser with time.

5. Conclusions

In the current study, the numerical simulation framework, GeoMicro3D, has been extended to model the hydration and microstructural development of a one-part geopolymer, which contains slag, K_2SiO_3, micro silica, and granite. The extended framework is capable of simulating the dissolution of different components in the solution, transportation of ions in the microstructure, and precipitating reaction products with the aid of thermodynamic modeling. The major conclusions from the current study are:

1. The initial input microstructure is built using the Anm model, considering the real shape of the particles and particle size distribution of the solid components, i.e., slag, K_2SiO_3, micro silica, and granite.
2. The forward dissolution rate of different elements from slag (Si, Ca, and Al), micro-silica (Si), K_2SiO_3 (Si) materials are calculated from the dissolution experiments, which are further used as input for GeoMicro3D.
3. The precipitation of the products in the microstructure of the paste is modeled using classical nucleation probability and thermodynamic modeling which can quantitatively predict the formation of different reaction products such as C-(N,*K*)-A-S-H, Nat(K), Natrolite and MA-OH-LDH in the microstructure.
4. The DOR of slag and volume of reaction products are estimated using SEM-BSE. The simulated DOR for slag and volume of reaction products shows good agreement with the experiments, proving the rationality of the model.

CRediT authorship contribution statement

Mayank Gupta: Writing – original draft, Validation, Software, Methodology, Investigation, Formal analysis, Data curation, Conceptualization. **Xiujiao Qiu:** Writing – review & editing, Validation, Software, Methodology, Investigation, Data curation, Conceptualization. **Mohamed Omran:** Writing – review & editing, Formal analysis, Data curation. **Yun Chen:** Writing – review & editing, Validation. **Mahmoud Khalifeh:** Writing – review & editing, Supervision, Funding acquisition. **Guang Ye:** Writing – review & editing, Supervision, Funding acquisition.

Declaration of competing interest

The authors declare that they have no known competing financial interests or personal relationships that could have appeared to influence the work reported in this paper.

Acknowledgment

The authors acknowledge the CEMENTEGRITY project that is funded through the ACT program (Accelerating CCS Technologies, Horizon2020 Project No 691712).

Data availability

Data will be made available on request.

References

[1] R. Nataly Echevarria Huaman, T. Xiu Jun, Energy related CO2 emissions and the progress on CCS projects: a review, Renew. Sust. Energ. Rev. 31 (2014) 368–385, https://doi.org/10.1016/j.rser.2013.12.002.
[2] R. Wennersten, Q. Sun, H. Li, The future potential for carbon capture and storage in climate change mitigation – an overview from perspectives of technology, economy and risk, J. Clean. Prod. 103 (2015) 724–736, https://doi.org/10.1016/j.jclepro.2014.09.023.
[3] C.B. Field, V.R. Barros, Climate Change 2014–Impacts, Adaptation and Vulnerability: Global and Sectoral Aspects, Cambridge University Press, 2014.
[4] T. Stocker, Climate Change 2013: The Physical Science Basis: Working Group I Contribution to the Fifth Assessment Report of the Intergovernmental Panel on Climate Change, Cambridge university press, 2014.
[5] M. Bai, Z. Zhang, X. Fu, A review on well integrity issues for CO2 geological storage and enhanced gas recovery, Renew. Sust. Energ. Rev. 59 (2016) 920–926, https://doi.org/10.1016/j.rser.2016.01.043.
[6] J. Iyer, G. Lackey, L. Edvardsen, A. Bean, S.A. Carroll, N. Huerta, M.M. Smith, M. Torsæter, R.M. Dilmore, P. Cerasi, A review of well integrity based on Field experience at carbon utilization and storage sites, Int. J. Greenhouse Gas Control 113 (2022), https://doi.org/10.1016/j.ijggc.2021.103533.
[7] R. Kiran, C. Teodoriu, Y. Dadmohammadi, R. Nygaard, D. Wood, M. Mokhtari, S. Salehi, Identification and evaluation of well integrity and causes of failure of well integrity barriers (a review), J. Nat. Gas Sci. Eng. 45 (2017) 511–526, https://doi.org/10.1016/j.jngse.2017.05.009.
[8] S.H. Hajiabadi, M. Khalifeh, R. van Noort, P.H. Silva Santos Moreira, Review on Geopolymers as wellbore sealants: state of the art optimization for CO $_2$ exposure and perspectives, ACS Omega 8 (2023) 23320–23345, https://doi.org/10.1021/acsomega.3c01777.
[9] N. Gaurina-Medjimurec, B. Pasic, CO2 underground storage and wellbore integrity, in: Risk Analysis for Prevention of Hazardous Situations in Petroleum and Natural Gas Engineering, IGI Global, 2014: pp. 322–357.
[10] A. Raza, R. Rezaee, R. Gholami, V. Rasouli, C.H. Bing, R. Nagarajan, M.A. Hamid, Injectivity and quantification of capillary trapping for CO 2 storage: a review of influencing parameters, J. Nat. Gas Sci. Eng. 26 (2015) 510–517, https://doi.org/10.1016/j.jngse.2015.06.046.
[11] V. BARLETGOUEDARD, G. RIMMELE, O. PORCHERIE, N. QUISEL, J. DESROCHES, A solution against well cement degradation under CO2 geological storage environment, Int. J. Greenhouse Gas Control 3 (2009) 206–216, https://doi.org/10.1016/j.ijggc.2008.07.005.
[12] L.K. Turner, F.G. Collins, Carbon dioxide equivalent (CO2-e) emissions: a comparison between geopolymer and OPC cement concrete, Constr. Build. Mater. 43 (2013) 125–130, https://doi.org/10.1016/j.conbuildmat.2013.01.023.
[13] Ø. Brandvoll, O. Regnault, I.A. Munz, I.K. Iden, H. Johansen, Fluid–solid interactions related to subsurface storage of CO2 experimental tests of well cement, Energy Procedia 1 (2009) 3367–3374, https://doi.org/10.1016/j.egypro.2009.02.125.
[14] M. Kamali, M. Khalifeh, E. Eid, A. Saasen, Experimental study of hydraulic Sealability and shear bond strength of cementitious barrier materials, J. Energy Resour. Technol. 144 (2022), https://doi.org/10.1115/1.4051269.
[15] K. Sedić, N. Ukrainczyk, V. Mandić, N. Gaurina-Međimurec, Carbonation study of new calcium aluminate cement-based CO2 injection well sealants, Constr. Build. Mater. 419 (2024) 135517, https://doi.org/10.1016/j.conbuildmat.2024.135517.
[16] K. Li, A.M.H. Pluymakers, Effects of thermal shocks on integrity of existing and newly-designed sealants for CCS applications, Int. J. Greenhouse Gas Control 133 (2024) 104103, https://doi.org/10.1016/j.ijggc.2024.104103.
[17] M.C.M. Nasvi, T.D. Rathnaweera, E. Padmanabhan, Geopolymer as well cement and its mechanical integrity under deep down-hole stress conditions: application for carbon capture and storage wells, Geomech. Geophys. Geo-Energy Geo-Resour. 2 (2016) 245–256, https://doi.org/10.1007/s40948-016-0034-2.
[18] M.C.M. Nasvi, P.G. Ranjith, J. Sanjayan, A. Haque, X. Li, Mechanical behaviour of wellbore materials saturated in brine water with different salinity levels, Energy 66 (2014) 239–249, https://doi.org/10.1016/j.energy.2013.12.003.
[19] T. Bakharev, Resistance of geopolymer materials to acid attack, Cem. Concr. Res. 35 (2005) 658–670, https://doi.org/10.1016/j.cemconres.2004.06.005.
[20] M.R. Ahmad, B. Chen, S.F.A. Shah, Influence of different admixtures on the mechanical and durability properties of one-part alkali-activated mortars, Constr. Build. Mater. 265 (2020) 120320, https://doi.org/10.1016/j.conbuildmat.2020.120320.
[21] A. Wang, Y. Zheng, Z. Zhang, K. Liu, Y. Li, L. Shi, D. Sun, The durability of alkali-activated materials in comparison with ordinary Portland cements and concretes: a

review, Engineering 6 (2020) 695–706, https://doi.org/10.1016/j.eng.2019.08.019.
[22] M. Khalifeh, J. Todorovic, T. Vrålstad, A. Saasen, H. Hodne, Long-term durability of rock-based geopolymers aged at downhole conditions for oil well cementing operations, J. Sustain. Cem.-Based Mater. 6 (2017) 217–230, https://doi.org/10.1080/21650373.2016.1196466.
[23] S.H. Hajiabadi, M. Khalifeh, R. van Noort, Multiscale insights into mechanical performance of a granite-based geopolymer: unveiling the micro to macro behavior, Geoenergy Sci. Eng. 231 (2023) 212375, https://doi.org/10.1016/j.geoen.2023.212375.
[24] S.H. Hajiabadi, M. Khalifeh, R. Van Noort, P.H.S.S. Moreira, Effect of magnesium-bearing additives on the properties of a granite-based geopolymer sealant for CCS, in: In: 84th EAGE Annual Conference & Exhibition, European Association of Geoscientists & Engineers, 2023, pp. 1–5, https://doi.org/10.3997/2214-4609.202310742.
[25] E. Eid, H. Tranggono, M. Khalifeh, S. Salehi, A. Saasen, Impact of drilling fluid contamination on performance of rock-based geopolymers, SPE J. 26 (2021) 3626–3633.
[26] S.H. Hajiabadi, M. Khalifeh, R. van Noort, Stability analysis of a granite-based geopolymer sealant for CO2 geosequestration: in-situ permeability and mechanical behavior while exposed to brine, Cem. Concr. Compos. 149 (2024) 105511, https://doi.org/10.1016/j.cemconcomp.2024.105511.
[27] F.D. Gomado, M. Khalifeh, M. Kamali, A. Saasen, J.A. Aasen, Sealing Performance of Geopolymer for Plugging and Abandonment; Apple-to-Apple Scenario, in: Day 1 Wed, April 27, 2022, SPE, 2022, https://doi.org/10.2118/209552-MS.
[28] M. Recasens, S. Garcia, E. Mackay, J. Delgado, M.M. Maroto-Valer, Experimental study of wellbore integrity for CO2 geological storage, Energy Procedia 114 (2017) 5249–5255, https://doi.org/10.1016/j.egypro.2017.03.1681.
[29] S. Mito, Z. Xue, H. Satoh, Experimental assessment of well integrity for CO2 geological storage: batch experimental results on geochemical interactions between a CO2–brine mixture and a sandstone–cement–steel sample, Int. J. Greenhouse Gas Control 39 (2015) 420–431, https://doi.org/10.1016/j.ijggc.2015.06.007.
[30] C. Teodoriu, O. Bello, A review of cement testing apparatus and methods under CO2 environment and their impact on well integrity prediction – Where do we stand? J. Pet. Sci. Eng. 187 (2020) 106736 https://doi.org/10.1016/j.petrol.2019.106736.
[31] K. Van Breugel, Simulation of hydration and formation of structure in hardening cement-based materials., (1993).
[32] G. Ye, Experimental Study and Numerical Simulation of the Development of the Microstructure and Permeability of Cementitious Materials, 2003.
[33] D.P. Bentz, Three-dimensional computer simulation of Portland cement hydration and microstructure development, J. Am. Ceram. Soc. 80 (1997) 3–21, https://doi.org/10.1111/j.1151-2916.1997.tb02785.x.
[34] S. Bishnoi, K.L. Scrivener, μic: a new platform for modelling the hydration of cements, Cem. Concr. Res. 39 (2009) 266–274, https://doi.org/10.1016/j.cemconres.2008.12.002.
[35] Y. Zuo, G. Ye, GeoMicro3D: a novel numerical model for simulating the reaction process and microstructure formation of alkali-activated slag, Cem. Concr. Res. 141 (2021) 106328, https://doi.org/10.1016/j.cemconres.2020.106328.
[36] Y. Zuo, G. Ye, Lattice Boltzmann simulation of the dissolution of slag in alkaline solution using real-shape particles, Cem. Concr. Res. 140 (2021) 106313, https://doi.org/10.1016/j.cemconres.2020.106313.
[37] M.D. Abràmoff, P.J. Magalhães, S.J. Ram, Image processing with ImageJ, Biophoton. Int. 11 (2004) 36–42.
[38] Z. Qian, E.J. Garboczi, G. Ye, E. Schlangen, Anm: a geometrical model for the composite structure of mortar and concrete using real-shape particles, Mater. Struct. 49 (2016) 149–158, https://doi.org/10.1617/s11527-014-0482-5.
[39] E.J. Garboczi, Three-dimensional mathematical analysis of particle shape using X-ray tomography and spherical harmonics: application to aggregates used in concrete, Cem. Concr. Res. 32 (2002) 1621–1638, https://doi.org/10.1016/S0008-8846(02)00836-0.
[40] M.A. Taylor, E.J. Garboczi, S.T. Erdogan, D.W. Fowler, Some properties of irregular 3-D particles, Powder Technol. 162 (2006) 1–15, https://doi.org/10.1016/j.powtec.2005.10.013.
[41] Z. Qian, E. Schlangen, G. Ye, K. Van Breugel, Modeling framework for fracture in multiscale cement-based material structures, Materials 10 (2017) 587, https://doi.org/10.3390/ma10060587.
[42] R. Snellings, Solution-controlled dissolution of supplementary cementitious material glasses at pH 13: the effect of solution composition on glass dissolution rates, J. Am. Ceram. Soc. 96 (2013) 2467–2475, https://doi.org/10.1111/jace.12480.
[43] A. Schöler, F. Winnefeld, M. Ben Haha, B. Lothenbach, The effect of glass composition on the reactivity of synthetic glasses, J. Am. Ceram. Soc. 100 (2017) 2553–2567, https://doi.org/10.1111/jace.14759.
[44] B. Lothenbach, D.A. Kulik, T. Matschei, M. Balonis, L. Baquerizo, B. Dilnesa, G. D. Miron, R.J. Myers, Cemdata18: a chemical thermodynamic database for hydrated Portland cements and alkali-activated materials, Cem. Concr. Res. 115 (2019) 472–506, https://doi.org/10.1016/j.cemconres.2018.04.018.
[45] E.H. Oelkers, General kinetic description of multioxide silicate mineral and glass dissolution, Geochim. Cosmochim. Acta 65 (2001) 3703–3719, https://doi.org/10.1016/S0016-7037(01)00710-4.
[46] E.H. Oelkers, J. Schott, J.-L. Devidal, The effect of aluminum, pH, and chemical affinity on the rates of aluminosilicate dissolution reactions, Geochim. Cosmochim. Acta 58 (1994) 2011–2024, https://doi.org/10.1016/0016-7037(94)90281-X.
[47] Y. Niibori, M. Kunita, O. Tochiyama, T. Choda, Dissolution rates of amorphous silica in highly alkaline solution, J. Nucl. Sci. Technol. 37 (2000) 349–357, https://doi.org/10.1080/18811248.2000.9714905.
[48] A. Packter, H.S. Dhillon, Studies on recrystallised aluminium hydroxide precipitates, Colloid Polym. Sci. 252 (1974) 249–256, https://doi.org/10.1007/BF01638106.
[49] T. Stamatis, M. Aggeliki, Hydration of CaO present in fly ashes 1039, National Technical University of Athens, 2015, pp. 1–74.
[50] Y. Zuo, Experimental Study and Numerical Simulation of the Reaction Process and Microstructure Formation of Alkali-Activated Materials, 2019.
[51] L. Li, R. Mei, J.F. Klausner, Multiple-relaxation-time lattice Boltzmann model for the axisymmetric convection diffusion equation, Int. J. Heat Mass Transf. 67 (2013) 338–351, https://doi.org/10.1016/j.ijheatmasstransfer.2013.08.039.
[52] H. Yoshida, M. Nagaoka, Multiple-relaxation-time lattice Boltzmann model for the convection and anisotropic diffusion equation, J. Comput. Phys. 229 (2010) 7774–7795, https://doi.org/10.1016/j.jcp.2010.06.037.
[53] Z. Chai, C. Huang, B. Shi, Z. Guo, A comparative study on the lattice Boltzmann models for predicting effective diffusivity of porous media, Int. J. Heat Mass Transf. 98 (2016) 687–696, https://doi.org/10.1016/j.ijheatmasstransfer.2016.03.065.
[54] E.L. Cussler, Diffusion: Mass Transfer in Fluid Systems, Cambridge university press, 2009.
[55] H. Huang, Thermodynamics of Autogenous Self-Healing in Cementitious Materials, Delft University of Technology, Delft, 2014.
[56] E.J. Garboczi, D.P. Bentz, Computer simulation of the diffusivity of cement-based materials, J. Mater. Sci. 27 (1992) 2083–2092, https://doi.org/10.1007/BF01117921.
[57] S. Jiang, J.H. ter Horst, Crystal nucleation rates from probability distributions of induction times, Cryst. Growth Des. 11 (2011) 256–261, https://doi.org/10.1021/cg101213q.
[58] D. Kashchiev, G.M. van Rosmalen, Review: nucleation in solutions revisited, Cryst. Res. Technol. 38 (2003) 555–574, https://doi.org/10.1002/crat.200310070.
[59] R.J. Myers, S.A. Bernal, J.L. Provis, A thermodynamic model for C-(N-)A-S-H gel: CNASH_ss. Derivation and validation, Cem. Concr. Res. 66 (2014) 27–47, https://doi.org/10.1016/j.cemconres.2014.07.005.
[60] A. Roy, P.J. Schilling, H.C. Eaton, P.G. Malone, W.N. Brabston, L.D. Wakeley, Activation of ground blast-furnace slag by alkali-metal and alkaline-earth hydroxides, J. Am. Ceram. Soc. 75 (1992) 3233–3240, https://doi.org/10.1111/j.1151-2916.1992.tb04416.x.
[61] G.D. Miron, D.A. Kulik, Y. Yan, J. Tits, B. Lothenbach, Extensions of CASH+ thermodynamic solid solution model for the uptake of alkali metals and alkaline earth metals in C-S-H, Cem. Concr. Res. 152 (2022) 106667, https://doi.org/10.1016/j.cemconres.2021.106667.
[62] R.J. Myers, E. L'Hôpital, J.L. Provis, B. Lothenbach, Composition–solubility–structure relationships in calcium (alkali) aluminosilicate hydrate (C-(N,K-)A-S-H), Dalton Trans. 44 (2015) 13530–13544, https://doi.org/10.1039/C5DT01124H.
[63] R.J. Myers, B. Lothenbach, S.A. Bernal, J.L. Provis, Thermodynamic modelling of alkali-activated slag cements, Appl. Geochem. 61 (2015) 233–247, https://doi.org/10.1016/j.apgeochem.2015.06.006.
[64] R.k. Allada, Thermochemistry of hydrotalcite-like phases in the MgO-Al2O3-CO2-H2O system: a determination of enthalpy, entropy, and free energy, Am. Mineral. 90 (2005) 329–335, https://doi.org/10.2138/am.2005.1737.
[65] I.G. Richardson, Clarification of possible ordered distributions of trivalent cations in layered double hydroxides and an explanation for the observed variation in the lower solid-solution limit, Acta Crystallogr. Sect. B: Struct. Sci. Cryst. Eng. Mater. 69 (2013) 629–633, https://doi.org/10.1107/S2052519213027905.
[66] B. Ma, B. Lothenbach, Synthesis, characterization, and thermodynamic study of selected K-based zeolites, Cem. Concr. Res. 148 (2021) 106537, https://doi.org/10.1016/j.cemconres.2021.106537.
[67] B. Ma, B. Lothenbach, Synthesis, characterization, and thermodynamic study of selected Na-based zeolites, Cem. Concr. Res. 135 (2020) 106111, https://doi.org/10.1016/j.cemconres.2020.106111.
[68] T. Wagner, D.A. Kulik, F.F. Hingerl, S.V. Dmytrieva, GEM-Selektor geochemical modeling package: TSolMod library and data interface for multicomponent phase models, Can. Mineral. 50 (2012) 1173–1195.
[69] D.A. Kulik, T. Wagner, S.V. Dmytrieva, G. Kosakowski, F.F. Hingerl, K. V. Chudnenko, U.R. Berner, GEM-Selektor geochemical modeling package: revised algorithm and GEMS3K numerical kernel for coupled simulation codes, Comput. Geosci. (2012), https://doi.org/10.1007/s10596-012-9310-6.
[70] Y. Inagaki, T. Kikunaga, K. Idemitsu, T. Arima, Initial dissolution rate of the international simple glass as a function of <scp>pH</scp> and temperature measured using microchannel flow-through test method, Int. J. Appl. Glas. Sci. 4 (2013) 317–327, https://doi.org/10.1111/ijag.12043.
[71] B. Grambow, R. Müller, First-order dissolution rate law and the role of surface layers in glass performance assessment, J. Nucl. Mater. 298 (2001) 112–124, https://doi.org/10.1016/S0022-3115(01)00619-5.
[72] E.H. Oelkers, An experimental study of forsterite dissolution rates as a function of temperature and aqueous mg and Si concentrations, Chem. Geol. 175 (2001) 485–494, https://doi.org/10.1016/S0009-2541(00)00352-1.
[73] X. Cheng, R.K. Brow, G. Chen, The dissolution behavior in alkaline solutions of a borosilicate glass with and without P_2O_5, J. Am. Ceram. Soc. 100 (2017) 4519–4532, https://doi.org/10.1111/jace.14933.
[74] B.C. Bunker, Molecular mechanisms for corrosion of silica and silicate glasses, J. Non-Cryst. Solids 179 (1994) 300–308, https://doi.org/10.1016/0022-3093(94)90708-0.

[75] Y. Zuo, M. Nedeljković, G. Ye, Pore solution composition of alkali-activated slag/fly ash pastes, Cem. Concr. Res. 115 (2019) 230–250, https://doi.org/10.1016/j.cemconres.2018.10.010.
[76] B. Lothenbach, F. Winnefeld, C. Alder, E. Wieland, P. Lunk, Effect of temperature on the pore solution, microstructure and hydration products of Portland cement pastes, Cem. Concr. Res. 37 (2007) 483–491, https://doi.org/10.1016/j.cemconres.2006.11.016.
[77] G. Plusquellec, M.R. Geiker, J. Lindgård, J. Duchesne, B. Fournier, K. De Weerdt, Determination of the pH and the free alkali metal content in the pore solution of concrete: review and experimental comparison, Cem. Concr. Res. 96 (2017) 13–26, https://doi.org/10.1016/j.cemconres.2017.03.002.